PHYSICAL REVIEW D **90,** 103519 (2014)

Statistics of cosmic density profiles from perturbation theory

Francis Bernardeau,[1,2] Christophe Pichon,[2,3,4] and Sandrine Codis[2]
[1]*Institut de Physique Théorique, CEA, IPhT, F-91191 Gif-sur-Yvette,*
CNRS, URA 2306, F-91191 Gif-sur-Yvette, France
[2]*Institut d'Astrophysique de Paris and UPMC (UMR 7095), 98 bis boulevard Arago, 75014 Paris, France*
[3]*Institute of Astronomy, University of Cambridge, Madingley Road,*
Cambridge CB3 0HA, United Kingdom
[4]*KITP Kohn Hall-4030 University of California, Santa Barbara, California 93106-4030, USA*
(Received 11 November 2013; published 14 November 2014)

The joint probability distribution function (PDF) of the density within multiple concentric spherical cells is considered. It is shown how its cumulant generating function can be obtained at tree order in perturbation theory as the Legendre transform of a function directly built in terms of the initial moments. In the context of the upcoming generation of large-scale structure surveys, it is conjectured that this result correctly models such a function for finite values of the variance. Detailed consequences of this assumption are explored. In particular the corresponding one-cell density probability distribution at finite variance is computed for realistic power spectra, taking into account its scale variation. It is found to be in agreement with Λ-cold dark matter simulations at the few percent level for a wide range of density values and parameters. Related explicit analytic expansions at the low and high density tails are given. The conditional (at fixed density) and marginal probability of the slope—the density difference between adjacent cells—and its fluctuations is also computed from the two-cell joint PDF; it also compares very well to simulations. It is emphasized that this could prove useful when studying the statistical properties of voids as it can serve as a statistical indicator to test gravity models and/or probe key cosmological parameters.

DOI: 10.1103/PhysRevD.90.103519 PACS numbers: 98.80.-k, 98.65.-r

I. INTRODUCTION

With new generations of surveys either from ground-based facilities (e.g. BigBOSS, DES, Pan-STARRS, LSST [1]) or space-based observatories (EUCLID [2], SNAP and JDEM [3]), it will be possible to test with unprecedented accuracy the details of gravitational instabilities, in particular as it enters the nonlinear regime. These confrontations can be used in principle to test the gravity models (see for instance [4,5]) and/or more generally improve upon our knowledge of cosmological parameters as detailed in [2].

There are only a limited range of quantities that can be computed from first principles. Next-to-leading-order terms to power spectra and polyspectra have been investigated extensively over the last few years with the introduction of novel methods. Standard perturbation theory calculations, as described in [6], have indeed been extended by the development of alternative analytical methods that try to improve upon standard calculations. The first significant progress in this line of calculations in the renormalized perturbation theory proposition [7] followed by the closure theory [8] and the time flow equations approach [9]. Latest propositions, namely MPTbreeze [10] and RegPT [11], incorporate 2-loop-order calculations and are accompanied by publicly released codes. Recent developments involve the effective field theory approaches [12].

Alternatively one may look for more global properties of the fields that capture some aspects of their non-Gaussian nature. A number of tests have been put forward from peak statistics (see [13]) that set the stage for Gaussian fields, to topological invariants. The latter, introduced for instance in [14] or in [15], aim at producing robust statistical indicators. This topic was renewed in [16] and [17] with the introduction of the notion of a skeleton. How such observables are affected by weak deviations from Gaussianity was investigated originally in [18] and for instance more recently in [17,19] with the use of standard tools such as the Edgeworth expansion applied here to multiple variable distributions. These approaches, although promising, are hampered by the limited range of applicability of such expansions and as a consequence have to be restricted to a limited range of parameters and are usually confined to the nonrare event region.

There is however at least one counterexample to that general statement: the density probability distribution functions in concentric cells. As we will show in detail in the following it is possible to get a global picture of what the joint density probability distribution function (PDF) should be, including in its rare event tails. The size of the past surveys prevented an effective use of such statistical tools. Their current size makes it now possible to try and confront theoretical calculations with observations.

Hence the aim of the paper is to revisit these calculations and assess their domain of validity with the help of numerical simulations.

To a large extent, the mathematical foundations of the calculation of the density probability distribution functions in concentric cells are to be found in early works by Balian and Schaeffer [20], who explored the connection between count-in-cell statistics and the properties of the cumulant generating functions. In that paper, the shape of the latter was just assumed without direct connection with the dynamical equations. This connection was established in [21] where it was shown that the leading order generating function of the count-in-cell probability distribution function could be derived from the dynamical equations. More precise calculations were developed in a systematic way in [22] that takes into account filtering effects, as pioneered in [23,24] where the impact of a Gaussian window function or a top-hat window function was taken into account. At the same time, these predictions were subjected to simulations and shown to be in excellent agreement with the numerical results (see for instance [22,25]). We will revisit here the quality of these predictions with the help of more accurate simulations. In parallel, it was shown that the same formalism could address more varied situations: large-scale biasing in [26], projection effects in [27,28]. A comprehensive presentation of these early works can be found in [6].

Insights into the theoretical foundations of this approach were presented in [29] that allow to go beyond the diagrammatic approach that was initially employed. The key argument is that for densities in concentric cells, *the leading contributions* in the implementation of the steepest descent method to the integration over field configurations should be configurations *that are spherically symmetric*. One can then take advantage of Gauss's theorem to map the final field configuration into the initial one with a finite number of initial variables, on a cell-by-cell basis. This is the strategy we adopt below. The purpose of this work is to rederive the fundamental relation that was obtained by the above mentioned authors, and to revisit the practical implementation of these calculations alleviating some of the shortcuts that were used in the literature.

Specifically, the first objective of this paper is to quantity the sensitivity of the predictions for the one-cell PDF for the density on the power spectrum shape, its index and the scale dependence of the latter (the so-called running parameter). The second objective is to show that it is possible to use the two-cell formalism to derive the statistical properties of the density *slope* defined as the difference of the density in two concentric cells of (possibly infinitesimally) close radii and more globally the whole density profile. More specifically we show that for sufficiently steep power spectra (index less than -1), it is possible to take the limit of infinitely close top-hat radii and define the density slope at a given radius. We can then take advantage of this machinery to derive low-order cumulants of this quantity as well as its complete PDF. Finally this investigation allows us to make a theoretical connection with recent efforts (see for instance [30–36]) in exploring the low density regions and their properties [37] such as the constrained average slope and its fluctuations given the (possibly low) value of the local density. This opens the way to exploit the properties of low density regions: we will suggest that the expected profile of low density regions is in fact a robust tool to use when matching theoretical predictions to catalogs.

The outline of the paper is the following. In Sec. II we present the general formalism of how the cumulant generating functions are related to the spherical collapse dynamics. In Sec. III, this relationship is applied to derive the one-point-density PDF; the sensitivity of the predictions with scale and with the power spectrum shape is also reviewed there. In Sec. IV, we define the density profile and the slope, and derive its statistical properties. A summary and discussion on the scope of these results is given in the last section.

II. THE CUMULANT GENERATING FUNCTION AT TREE ORDER

Let us first revisit the derivation of the tree-order cumulant generating functions for densities computed in concentric cells.

A. Definitions and connections to spherical collapse

We consider a cosmological density field, $\rho(\mathbf{x})$, which is statically isotropic and homogeneous. The average value of $\rho(\mathbf{x})$ is set to unity. We then consider a random position $\mathbf{x}_0$ and n concentric cells of radius R_i centered on $\mathbf{x}_0$. The densities, ρ_i, obtained as the density within the radius R_i,

$$\rho_i = \frac{1}{4\pi R_i^3/3}\int_{|\mathbf{x}-\mathbf{x}_0|<R_i} d^3\mathbf{x}\,\rho(\mathbf{x}), \tag{1}$$

form a set of correlated random variables. For a nonlinearly evolved cosmic density field, they display non-Gaussian statistical properties. It is therefore natural to define the generating function of their joint moments as

$$\mathcal{M}(\{\lambda_k\}) = \sum_{p_i=0}^{\infty}\langle\Pi_i\rho_i^{p_i}\rangle\frac{\Pi_i\lambda_i^{p_i}}{\Pi_i p_i!}, \tag{2}$$

which can be simply expressed as

$$\mathcal{M}(\{\lambda_k\}) = \left\langle\exp\left(\sum_i\lambda_i\rho_i\right)\right\rangle. \tag{3}$$

The generating function, $\mathcal{M}(\{\lambda_k\})$, is a function of the n variables λ_k. A very general theorem (see for instance [38,39]) states that this generating function is closely related to the joint *cumulant* generating function,

$$\varphi(\{\lambda_k\}) = \sum_{p_i=0}^{\infty}\langle\Pi_i\rho_i^{p_i}\rangle_c\frac{\Pi_i\lambda_i^{p_i}}{\Pi_i p_i!}, \tag{4}$$

via the relation

$$\mathcal{M}(\{\lambda_k\}) = \exp[\varphi(\{\lambda_k\})]. \tag{5}$$

Note importantly that this makes $\varphi(\{\lambda_k\})$ an observable on its own [40].

The tree-order expression of such cumulants can be derived from a direct expansion of the density field, i.e.

$$\rho(\mathbf{x}) = 1 + \delta^{(1)} + \delta^{(2)} + \delta^{(3)} + \cdots, \tag{6}$$

where $\delta^{(p)}$ is of order p with respect to the initial density contrast. For Gaussian initial conditions the leading order cumulant (that is the connected parts of the moments) can be derived from the expression of the fields $\delta^{(p)}$. Formally, Wick's theorem imposes [41] that the leading contributions to the p-order cumulant obtained from the following terms:

$$\langle \rho^p \rangle_c = \sum_{\sum_{i=1}^p n_i = 2(p-1)} \langle \Pi_{i=1}^p \delta^{(n_i)} \rangle_c. \tag{7}$$

One of the well-known consequences of that property is that $\langle \rho^p \rangle_c$ scales like $\langle \rho^2 \rangle_c^{2(p-1)}$. It is then natural to define precisely the reduced cumulants, S_p, as

$$S_p(\eta) = \frac{\langle \rho_i^p \rangle_c}{\langle \rho_i^2 \rangle_c^{2(p-1)}}. \tag{8}$$

It has been shown in [21,22] that these quantities are entirely determined by the dynamics of the spherical collapse. More precisely the function ζ that relates the initial density contrast $\tau_{<r}$ within a given shell of radius r to the time-dependent (η) nonlinear density contrast, $\rho_{<R}$ within the shell of radius $R = r\rho_{<R}^{-1/3}$,

$$\rho_{<R} = \zeta(\eta, \tau(<r)), \tag{9}$$

encodes all the necessary ingredients to compute the tree-order cumulants. Note that the mere existence of such a function takes full advantage of Gauss's theorem, as the time evolution of the shell radius depends only on the density contrast at this radius (before shell crossings). More precisely, if one perturbatively expands $\zeta(\eta, \tau)$ with respect to τ,

$$\zeta(\eta, \tau) = \sum_p \nu_p(\eta) \frac{(D_+(\eta)\tau)^p}{p!}, \tag{10}$$

where $D_+(\eta)$ is the linear growth factor between the initial time and time η (with $\nu_0 = 1$, $\nu_1 = 1$), then each $S_p(\eta)$ parameters can be expressed in terms of $\nu_p(\eta)$. For instance

$$S_3(\eta) = 3\nu_2(\eta) + \frac{\mathrm{d}\log\langle \tau^2(r)\rangle}{\mathrm{d}\log r}, \tag{11}$$

$$S_4(\eta) = 4\nu_3(\eta) + 12\nu_2^2(\eta) + (14\nu_2(\eta) - 2)\frac{\mathrm{d}\log[\langle \tau^2(r)\rangle]}{\mathrm{d}\log r} + \frac{7}{3}\left(\frac{\mathrm{d}\log[\langle \tau^2(r)\rangle]}{\mathrm{d}\log r}\right)^2 + \frac{2}{3}\frac{\mathrm{d}^2\log[\langle \tau^2(r)\rangle]}{\mathrm{d}\log^2 r}. \tag{12}$$

The explicit form of $\zeta(\eta, \tau)$ or equivalently the values of $\nu_p(\eta)$ can *a priori* be predicted for any given cosmology. They depend on time—although very weakly—and take simple analytic forms for an Einstein–de Sitter background. For instance, for such a background, we then have $\nu_2 = 34/21$. A more general expression of $\zeta(\eta, \tau)$ can be found in [21,43,44]. In practice one can use a simple expression for $\zeta(\tau)$:

$$\zeta(\tau) = \frac{1}{(1 - D_+(\eta)\tau/\nu)^\nu}. \tag{13}$$

Here we choose $\nu = 21/13 \approx 1.6$ so that the high z skewness of the density contrast is exactly reproduced [45]. We checked that this choice of ν reproduces the exact spherical collapse dynamics for an Einstein–de Sitter background at a precision level of 0.5% from $\zeta = 0.3$ to $\zeta = 2.5$, which is typically the range of values we need to cover.

The understanding of the connection between the leading order statistical properties and the spherical collapse dynamics has been dramatically improved in [26,28,29] where it was realized that it could be extended to the cumulants of any number of concentric cells. We now turn to the presentation of these results.

B. General derivation

We are here interested in the leading order expression of $\varphi = \varphi(\{\lambda_k\})$ for a finite number of concentric cells. In this section we set the dimension of space to be D, having in mind that the formulas we derive should be valid for $D = 2$ or $D = 3$. For completeness, we sketch here the demonstration of the results and refer to [29] for further details. To derive such an expression let us introduce the joint density probability distribution functions, $\mathcal{P}(\{\rho_k\})d\rho_1 \ldots d\rho_n$, so that

$$\exp[\varphi(\{\lambda_k\})] = \int d\rho_1 \ldots d\rho_n \mathcal{P}(\{\rho_k\}) \exp\left(\sum_i \lambda_i \rho_i\right).$$

This expression can be written in terms of the statistical properties of the *initial* field. Let us define $\tau(\mathbf{x})$ as the initial density contrast. Formally the quantities ρ_i are all functionals of the field, $\tau(\mathbf{x})$ [46], so that the ensemble average of the previous equation can be written as

$$\exp[\varphi] = \int \mathcal{D}\tau(\mathbf{x})\mathcal{P}(\{\tau(\mathbf{x})\})\exp\left(\sum_i \lambda_i \rho_i(\{\tau(\mathbf{x})\})\right), \tag{14}$$

where we introduced the field distribution function, $\mathcal{P}(\{\tau(\mathbf{x})\})$, and the corresponding measure $\mathcal{D}(\{\tau(\mathbf{x})\})$. These are assumed to be known *a priori*. They depend on the initial conditions and in the following we will assume the initial field is Gaussian distributed [47].

We now turn to the calculation of the generating function at leading order when the overall variance, σ^2, at scale R_i, is small. The idea is to identify the initial field configurations that give the largest contribution to this integral. For convenience, let us assume that the field $\tau(\mathbf{x})$ can be described with a discrete number of variables τ_i. For Gaussian initial conditions, the expression of the joint probability distribution function of τ_i reads

$$\mathcal{P}(\{\tau_k\})d\tau_1 \ldots d\tau_p = \frac{\exp\left[-\Psi(\{\tau_k\})\right]}{\sqrt{(2\pi)^p / \det \Xi}} d\tau_1 \ldots d\tau_p, \tag{15}$$

with

$$\Psi(\{\tau_k\}) = \frac{1}{2}\sum_{ij} \Xi_{ij}\tau_i\tau_j, \tag{16}$$

where Ξ_{ij} is the *inverse* of the covariance matrix, Σ_{ij}, defined as

$$\Sigma_{ij} = \langle \tau_i \tau_j \rangle. \tag{17}$$

The key idea to transform Eq. (14) using Eq. (15) relies on using the steepest descent method. Details of the validity regime of this approach and its construction can be found in [29]. The integral we are interested in is then dominated by a specific field configuration for which the following stationary conditions are verified:

$$\sum_i \lambda_i \frac{\delta\rho_i(\{\tau_k\})}{\delta\tau_j} = \frac{\delta}{\delta\tau_j}\Psi(\{\tau_k\}), \tag{18}$$

for any value of j. Up to this point this is a very general construction. Let us now propose a solution to these stationary equations that is consistent with the class of spherically symmetric problems we are interested in. The main point is the following: the configurations that are solutions of this equation, that is the values of $\{\tau_k\}$, depend specifically on the choice of the functionals $\rho_i(\{\tau_k\})$. When these functionals correspond to spherically symmetric quantities, the corresponding configurations are also likely to be spherically symmetric. But then Gauss's theorem is making things extremely simple: *before shell crossing*, each of the final density ρ_i can indeed be expressed in terms of a *single* initial quantity, namely the linear density contrast of the cell centered on $\mathbf{x}_0$ that contained the same amount of matter in the initial density field. We denote τ_i the corresponding density contrast, which means that, following definition (9), we have

$$\rho_i = \zeta(\eta, \tau_i), \tag{19}$$

and τ_i is the amplitude of the initial density within a specific radius [49], r_i, which obeys $r_i = R_i \rho_i^{1/D}$ thanks to mass conservation. The specificity of this mapping implies in particular that

$$\frac{\delta\rho_i(\{\tau_k\})}{\delta\tau_j} = \delta_{ij}\zeta'(\tau_i), \tag{20}$$

so that the stationary conditions (18) now read

$$\lambda_j \zeta'(\tau_j) = \frac{\delta}{\delta\tau_j}\Psi(\{\tau_k\}). \tag{21}$$

Note that the no-shell crossing conditions imply that if $R_i < R_j$, then $r_i < r_j$, which in turn implies that

$$\rho_i < \rho_j (R_j/R_i)^D. \tag{22}$$

It follows that the parameter space $\{\rho_k\}$ is not fully accessible. In the specific example we explore in the following, this restriction is not significant, but it could be in some other cases.

We are now close to the requested expression for $\varphi(\{\lambda_k\})$ as we have

$$\exp\left[\varphi(\{\lambda_k\})\right] = \int \mathrm{d}\tau_1 \ldots \mathrm{d}\tau_n \mathcal{P}(\{\tau_k\})\exp\left(\sum_i \lambda_i \rho_i(\{\tau_k\})\right).$$

To get the leading order expression of this form for $\varphi(\{\lambda_k\})$, using the steepest descent method, one is simply requested to identify the quantities that are exponentiated. As a result we have

$$\varphi(\{\lambda_k\}) = \sum_i \lambda_i \rho_i - \Psi(\{\rho_k\}), \tag{23}$$

where ρ_i are determined by the stationary conditions (21). The latter can be written equivalently as

$$\lambda_i = \frac{\partial}{\partial\rho_i}\Psi(\{\rho_k\}), \tag{24}$$

when all quantities are expressed in terms of ρ_i. Equation (24) is the general expression that we will exploit in the following. Formally, note that (21)–(23) imply that $\varphi(\{\lambda_k\})$ is the Legendre transform of Ψ when the latter is seen as a function of ρ_i, that is

$$\Psi(\{\rho_k\}) = \frac{1}{2}\sum_{ij}\Xi_{ij}(\{\rho_k\})\tau(\rho_i)\tau(\rho_j), \tag{25}$$

where the functional form $\tau(\rho)$ is obtained from the inversion of (19) at a fixed time, and Ξ_{ij} is the inverse matrix of the cross-correlation of the density in cells of radius $R_i\rho_i^{1/D}$ [cf. Eq. (17)]:

$$\Sigma_{ij} = \left\langle \tau\left(< R_i\rho_i^{1/D}\right)\tau\left(< R_j\rho_j^{1/D}\right)\right\rangle, \tag{26}$$

$$\sum_j \Sigma_{ij}\Xi_{jk} = \delta_{ik}. \tag{27}$$

These coefficients therefore depend on the whole set of both radii R_i and densities ρ_i. From the properties of Legendre transform, it follows in particular that

$$\rho_i = \frac{\partial}{\partial\lambda_i}\varphi(\{\lambda_k\}). \tag{28}$$

Although known for more than a decade, Eqs. (23)–(28) and their consequences have not been exploited to their full power in the literature. This is partially what we intend to do in this paper and in subsequent ones. For now, in order to get better acquainted with this formalism, let us first explore some of its properties.

C. General formalism

The relation Eqs. (23)–(28) have been derived for Gaussian initial conditions. This eases the presentation but it is not a key assumption. For instance in Eq. (15), $\Psi(\{\tau_k\})$ does not need to be quadratic in τ_k as for Gaussian initial conditions. If the initial conditions were to be non-Gaussian these features would have to be incorporated in the expression of $\Psi(\{\tau_k\})$. It would not however change the functional relation between $\varphi(\{\lambda_k\})$ and $\Psi(\{\tau_k\})$, provided $\Psi(\{\tau_k\})$ is properly defined when the variance is taken in its zero limit.

One can then observe that the Legendre transform between these two functions can be inverted [50]. Applying the fundamental relation at precisely the initial time, in a regime where $\rho_i \approx 1 + D_+(\eta)\tau_i$, will give the expression of the function $\Psi(\{\tau_k\})$ in terms of the initial cumulant generating function.

One can actually pursue this idea more generally. Let us define the nonlinear spherical transform $\zeta_\rho(\eta;\rho_0,\eta_0)$ that gives the value of the density ρ within a given radius R at time η knowing the density ρ_0 at time η_0 within radius $R_0 = R(\rho/\rho_0)^{1/3}$. It is obtained after τ has been eliminated in

$$\zeta_\rho(\eta;\rho_0,\eta_0) = \zeta(\eta,\tau), \tag{29}$$

$$\rho_0 = \zeta(\eta_0,\tau), \tag{30}$$

where ζ is defined in Eq. (9). Using the form (13), one gets

$$\zeta(\eta;\rho_0,\eta_0)^{-1/\nu} - 1 = \frac{D_+(\eta)}{D_+(\eta_0)}(\rho_0^{-1/\nu} - 1). \tag{31}$$

Incidentally we can note that the inverse function is obtained by changing η into η_0.

Then the general formulation of our result is that the Legendre transform of the joint cumulant generating function for a choice of radii R_k and taken at time η, which we denote here as $\Psi(\{(\rho_k,R_k)\},\eta)$, can be expressed in terms of the same Legendre transform taken at any other time, η',

$$\Psi(\{(\rho_k,R_k)\},\eta) = \Psi\left(\left\{\zeta_\rho(\eta';\rho_k,\eta), R_k\frac{\rho_k^{1/3}}{\zeta_\rho^{1/3}(\eta';\rho_k,\eta)}\right\},\eta'\right). \tag{32}$$

This is a general formalism that encompasses the result we just described [51] but can also be applied for any initial conditions or any time as it does refer explicitly to the initial conditions.

In this paper we will however use this construction for initial Gaussian conditions only with explicit use of the expressions derived in the previous subsection.

D. Scaling relations

It is interesting to note that the cumulant generating function has a simple dependence on the overall amplitude of the correlators σ_0^2. Let us denote in this subsection $\varphi_{\sigma_0}(\{\lambda_k\})$ the value of the cumulant generating function for a fixed value of σ_0. It is then straightforward to express $\varphi_{\sigma_0}(\{\lambda_k\})$ in terms of $\varphi_1(\{\lambda_k\})$, the expression of the generating function when σ_0 is set to unity. Indeed $\Psi(\{\rho_k\})$ is inversely proportional to σ_0^2 for fixed values of ρ_k. As a result λ_k scale like $1/\sigma_0^2$ for fixed values of $\{\rho_k\}$. Note that we have the following identity:

$$\varphi_{\sigma_0}(\{\lambda_k\}) = \frac{1}{\sigma_0^2}\varphi_1(\{\lambda_k/\sigma_0^2\}), \tag{33}$$

while the variables ρ_k are independent of σ_0.

In the upcoming applications we will make use of this property as we will keep the overall normalization as a free parameter—that will eventually be adjusted on numerical results, but will use the structural form of $\varphi_1(\{\lambda_k\})$ as predicted from the general theory. In particular this structural form depends on the specific shape of the power spectrum through the cross-correlation matrix Σ_{ij}.

E. The one-cell generating function

Turning back to the application of Eqs. (23)–(28), one obvious simple application corresponds to the one-cell characteristic function. In this case

$$\Psi(\rho) \equiv \frac{1}{2\sigma^2(R\rho^{1/D})}\tau(\rho)^2, \tag{34}$$

where

$$\sigma^2(r) = \langle \tau(<r)\tau(<r)\rangle. \tag{35}$$

The Legendre transform is then straightforward and $\varphi(\lambda)$ takes the form

$$\varphi(\lambda) = \lambda\rho - \frac{1}{2\sigma^2(R\rho^{1/D})}\tau(\rho)^2, \tag{36}$$

with ρ computed implicitly as a function of λ via Eq. (24). One way of rewriting this equation is to define $\tau_{\rm eff} = \tau\sigma(R)/\sigma(R\rho^{1/3})$ and the function $\zeta_{\rm eff}(\tau_{\rm eff})$ through the implicit form,

$$\zeta_{\rm eff}(\tau_{\rm eff}) = \zeta(\tau) = \zeta\left(\tau_{\rm eff}\frac{\sigma(R\zeta_{\rm eff}^{1/D})}{\sigma(R)}\right). \tag{37}$$

Then the expression of $\varphi(\lambda)$ is given by

$$\varphi(\lambda) = \lambda\rho - \frac{1}{2\sigma^2(R)}\tau_{\rm eff}^2, \tag{38}$$

with the stationary condition

$$\tau_{\rm eff} = \lambda\sigma^2\zeta'_{\rm eff}(\hat{\tau}). \tag{39}$$

In [22], the expression of the cumulant generating function was presented with this form. This is also the functional form one gets when one neglects the filtering effects (as was initially done in [21]) or for the so-called nonlinear hierarchical model used in [52]. Note that it is not possible however to use such a remapping for more than one cell. Note finally that this is a precious formulation for practical implementations, as one may rely on fitted forms for $\zeta_{\rm eff}$ to construct the generating function $\varphi(\lambda)$ while preserving its analytical properties. It is indeed always possible, once one has been able to numerically compute $\varphi(\lambda)$ for specific values of λ, to define $\zeta_{\rm eff}$ by Legendre transform and construct a fitted form with low-order polynomials while this is not possible for $\varphi(\lambda)$ which exhibits nontrivial analytical properties as we will see later on. This approach was used in [28]. It is also this procedure we use in Sec. IV for constructing the profile PDF.

F. Recovering the PDF via inverse Laplace transform

In the following we will exploit the expression for the cumulant generating function to get the one-point and joint density PDFs. To avoid confusion with the variables ρ_i that appear in the expression of Ψ, we will use the superscript $\hat{}$ to denote measurable densities, the PDF of which we wish to compute.

In general, the joint density PDF, $\mathcal{P} = \mathcal{P}(\hat{\rho}_1, \ldots, \hat{\rho}_n)$, that gives the probability that the densities within a set of n concentric cells of radii $R_1, \ldots, R_n$ are $\hat{\rho}_1, \ldots, \hat{\rho}_n$ within $d\hat{\rho}_1 \ldots d\hat{\rho}_n$ is given by

$$\mathcal{P} = \int_{-i\infty}^{+i\infty} \frac{{\rm d}\lambda_1}{2\pi i}\cdots\frac{{\rm d}\lambda_n}{2\pi i}\exp\left(-\sum_i \lambda_i\hat{\rho}_i + \varphi(\{\lambda_k\})\right). \tag{40}$$

where the integration in λ_i should be performed in the complex plane so as to maximize convergence. This equation defines the inverse Laplace transform of the cumulant generating function [53]. In the one-cell case, Eq. (40) simply reads

$$\mathcal{P}(\hat{\rho}_1) = \int_{-i\infty}^{+i\infty} \frac{{\rm d}\lambda_1}{2\pi i}\exp(-\lambda_1\hat{\rho}_1 + \varphi(\lambda_1)), \tag{41}$$

i.e. the PDF is the inverse Laplace transform of the one-variable moment generating function. This inversion is known to be tricky, and to our knowledge there are no known general foolproof methods. One practical difficulty is that it generically relies on the analytic continuation of the predicted cumulant generating function in the complex plane. It is therefore crucial to have a good knowledge of the analytic properties of $\varphi(\lambda)$, which is typically difficult since $\varphi(\lambda)$ is defined itself as the Legendre transform of $\Psi(\rho)$. Only a limited set of $\Psi(\rho)$ yield analytical $\varphi(\lambda)$, which in turn can be inverse Laplace transformed.

III. THE ONE-POINT PDF

Up to this point, the whole construction presented in the previous section would be a mere mathematical trick to compute explicit cumulants for top-hat window functions sparing the pain of lengthy integrations on wave modes. In this paper, we furthermore aim to use the cumulant generating function computed in the uniform limit $\Sigma_{ij} \to 0$ as an approximate form for the *exact* generating function when the Σ_{ij} are finite (but small). Note that this is a nontrivial extension for which we have no precise mathematical justifications. It assumes that the global properties of $\varphi(\{\lambda_k\})$—and in particular its analytical properties (which will be of crucial importance in the following)—should be meaningful for *finite values of* λ_k, and not only in the vicinity of $\{\lambda_k = 0\}$.

We now conjecture without further proof that they correctly represent the cumulant generating function for finite values of the variance.

A. General formulas and asymptotic forms

The implementation of the quadrature in Eq. (41) has been attempted in various papers [21,28,52], relying on different hypotheses for $\varphi(\lambda)$ [54]. Figure 1 yields a graphical representation of the stationary equation for a power law model with index $n = -1.5$. The implicit equation, $\Psi'[\rho] = \lambda$, always has a solution in the vicinity of $\rho \approx 0$. Expanding this equation around this point naturally gives the low-order cumulants at an arbitrary order.

Figure 1 shows graphically that there is a maximum value for λ, λ_c that can be reached, so that the Legendre transform of Ψ is not defined for $\lambda > \lambda_c$. It corresponds to a value $\rho = \rho_c$. At this location we have

$$0 = \Psi''[\rho_c], \qquad \lambda_c = \Psi'[\rho_c]. \tag{42}$$

Note that at $\rho = \rho_c$, Ψ is regular [in particular, the corresponding singular behavior in $\varphi(\lambda)$ is not related to any singularity of the spherical collapse dynamics]. The function $\varphi(\lambda)$ can be expanded at this point. In other words, Eq. (24) can be inverted as a series near (ρ_c, λ_c) [where Eq. (42) holds], and integrated for $\varphi(\lambda)$ using Eq. (28). We give here a whole set of subleading terms that we will take advantage of in the following,

$$\begin{aligned}\varphi(\lambda) = {} & \varphi_c + (\lambda-\lambda_c)\rho_c + \frac{2}{3}\sqrt{\frac{2}{\pi_3}}(\lambda-\lambda_c)^{3/2} - \frac{\pi_4(\lambda-\lambda_c)^2}{6\pi_3^2} \\ & + \frac{(\frac{1}{\pi_3})^{7/2}(5\pi_4^2 - 3\pi_3\pi_5)(\lambda-\lambda_c)^{5/2}}{45\sqrt{2}} - \frac{(40\pi_4^3 - 45\pi_3\pi_5\pi_4 + 9\pi_3^2\pi_6)(\lambda-\lambda_c)^3}{810\pi_3^5} \\ & + \frac{(\frac{1}{\pi_3})^{13/2}(385\pi_4^4 - 630\pi_3\pi_5\pi_4^2 + 168\pi_3^2\pi_6\pi_4 + 3\pi_3^2(35\pi_5^2 - 8\pi_3\pi_7))(\lambda-\lambda_c)^{7/2}}{7560\sqrt{2}} + \cdots,\end{aligned} \tag{43}$$

where $\pi_n = \partial^n\Psi/\partial\rho^n(\rho_c)$. It is to be noted that the leading singular term scales like $(\lambda-\lambda_c)^{3/2}$. The coefficients π_i are all related to the function Ψ and are therefore (cosmological) model dependent [55].

What are the consequences of this behavior for the PDF of the density? Let us present analytical forms for the inverse Laplace transform of $\exp\varphi$. The idea is that the inverse transform can be obtained via a saddle point approximation of Eq. (41) assuming the variance is small. Formally it leads to the conditions that should be met at the saddle point λ_s [56],

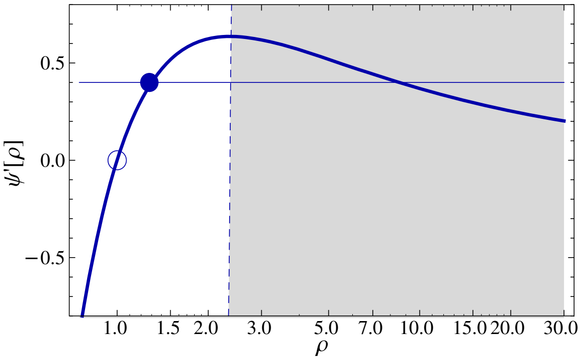

FIG. 1 (color online). A graphical representation of the one-dimensional stationary condition $\lambda = \Psi'[\rho]$. There is a maximum value for λ that corresponds to a critical value ρ_c for ρ defined in Eq. (42).

$$\frac{\partial}{\partial\lambda}[\lambda\hat{\rho} - \varphi(\lambda)] = 0, \tag{44}$$

$$\frac{\partial^2}{\partial\lambda^2}[\lambda\hat{\rho} - \varphi(\lambda)] < 0. \tag{45}$$

The first condition leads to $\rho(\lambda_s) = \hat{\rho}$, the second to $\lambda_s < \lambda_c$. This condition simply means that this approximation can be used if $\hat{\rho} < \rho_c$. The resulting simple expression for the density PDF is

$$\mathcal{P}(\hat{\rho}) = \frac{1}{\sqrt{2\pi}}\sqrt{\frac{\partial^2\Psi(\hat{\rho})}{\partial\hat{\rho}^2}}\exp[-\Psi(\hat{\rho})]. \tag{46}$$

It is valid as long as the expression that appears in the square root is positive, i.e. $\hat{\rho} < \rho_c$. When this condition is not satisfied, the singular behavior of φ near λ_c dominates the integral in the complex plane. This leads to the following expression for $\mathcal{P}(\hat{\rho})$ as described in Appendix B 2,

$$\begin{aligned}\mathcal{P}(\hat{\rho}) \approx \exp(\varphi_c - \lambda_c\hat{\rho})\Bigg(& \frac{3\Im(a_{\frac{3}{2}})}{4\sqrt{\pi}(\hat{\rho}-\rho_c)^{5/2}} + \frac{15\Im(a_{\frac{5}{2}})}{8\sqrt{\pi}(\hat{\rho}-\rho_c)^{7/2}} \\ & + \frac{105(\Im(a_{\frac{3}{2}})a_2 + \Im(a_{\frac{7}{2}}))}{16\sqrt{\pi}(\hat{\rho}-\rho_c)^{9/2}} + \cdots\Bigg),\end{aligned} \tag{47}$$

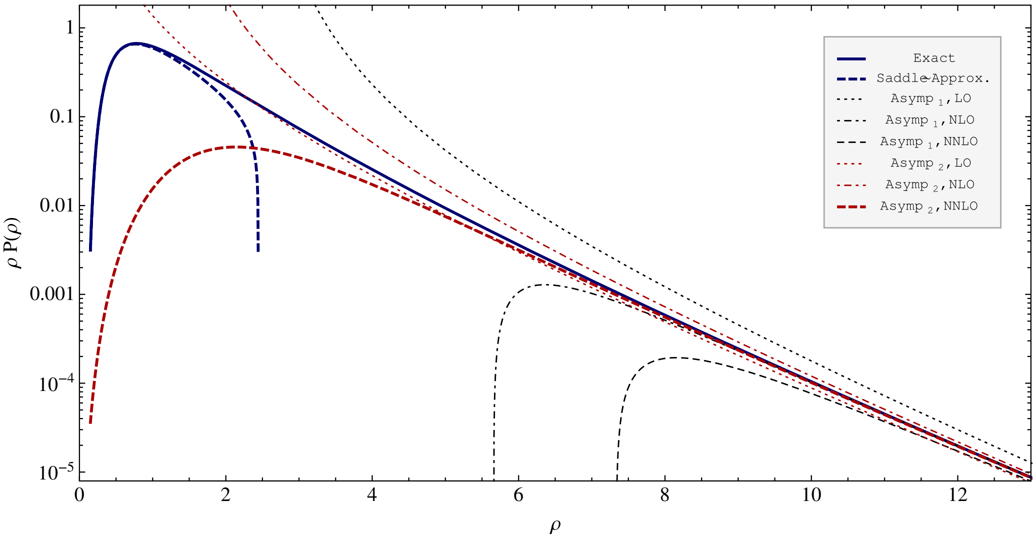

FIG. 2 (color online). The PDF of the one-point density. The blue solid line is the numerical integration, the red dashed line the low ρ asymptotic form of Eq. (46); the other lines correspond to the large ρ asymptotic forms proposed in the text: the dark lines correspond to the form (47) and the red lines to the form (48) and the forms are computed at leading order, at next-to-leading, and next-to-next-to-leading order for respectively the dotted, dot-dashed and dashed curves. The plots are given for $\sigma^2 = 0.45$ and a power law index of $n = -1.5$.

where a_j are the coefficients in front of $(\lambda - \lambda_c)^j$ in Eq. (43), (e.g. $a_{3/2} = 2/3\sqrt{2/\pi_3}$) and $\Im()$ is the imaginary part. Equation (47) has an exponential cutoff at large $\hat{\rho}$ scaling like $\exp(\lambda_c \hat{\rho})$. This property is actually robust and is preserved when one performs the inverse Laplace transform for finite values of the variance, or even large value of the variance (see [20,57]). It also gives a direct transcription of why $\varphi(\lambda)$ becomes singular: for values of λ that are larger than λ_c, the integral $\int \mathrm{d}\hat{\rho}\mathcal{P}(\hat{\rho})\exp(\lambda\hat{\rho})$ is not converging.

Note that in practice, it is best to rely on an alternative asymptotic form to Eq. (47) that is better behaved and remains finite for $\hat{\rho} \to \rho_c$. It is built in such a way that it has the same asymptotic behavior as Eq. (47) at a given order in the large ρ limit. The following form,

$$\mathcal{P}(\hat{\rho}) = \frac{3a_{\frac{3}{2}}\exp(\varphi_c - \lambda_c\hat{\rho})}{4\sqrt{\pi}(\hat{\rho} + r_1 + r_2/\hat{\rho} + \cdots)^{5/2}}, \tag{48}$$

where the r_i parameters are adjusted to fit the results of the previous expansion, proved very robust. At next-to-leading order (NLO) and next-to-next-to-leading order (NNLO) we have

$$r_1 = -\frac{\Im(a_{\frac{5}{2}})}{\Im(a_{\frac{3}{2}})} - \rho_c, \tag{49}$$

$$r_2 = -\frac{7(2a_2 a_{\frac{3}{2}}^2 + 2a_{\frac{7}{2}}a_{\frac{3}{2}} - a_{\frac{5}{2}}^2)}{4a_{\frac{3}{2}}^2}. \tag{50}$$

However, none of these asymptotic forms are accurate for the full range of density values; in general one has to rely on numerical integrations in the complex plane which can be done accurately and quickly, as described in Appendix B. The comparison between the analytical forms and the numerical integrations are shown in Fig. 2. Such comparisons are in fact conversely useful to assess the precision of the numerical integrations. Note that for the case explicitly shown, which corresponds to $\sigma^2 = 0.45$ and a power law index of $n = -1.5$, the asymptotic forms (46) and (48) at NNLO are valid within 2% everywhere but for the range $1 < \rho < 10$, where one must rely on an explicit integration in the complex plane.

B. Practical implementation, comparisons with N-body results

We now move to an explicit comparison of these predictions to N-body results. The simulations are described in Appendix D. They are determined in particular by the linear power spectrum $P^{\mathrm{lin}}(k)$ set for the initial conditions. The knowledge of the power spectrum determines the values of the cross-correlation matrix, $\Sigma_{ij}(R_i, R_j)$, that are explicitly given by

$$\Sigma_{ij} = \int \frac{\mathrm{d}^3\mathbf{k}}{(2\pi)^3} P^{\mathrm{lin}}(k) W_{3\mathrm{D}}(kR_i) W_{3\mathrm{D}}(kR_j), \tag{51}$$

where $W_{3\mathrm{D}}(k)$ is the shape of the top-hat window function in Fourier space,

$$W_{3\mathrm{D}}(k) = 3\sqrt{\frac{\pi}{2}} \frac{J_{3/2}(k)}{k^{3/2}}, \tag{52}$$

where $J_{3/2}(k)$ is the Bessel function of the first kind of index $3/2$. In three dimensions (3D), it is actually possible to express $W_{3\mathrm{D}}(k)$ in terms of elementary functions as

$$W_{3\mathrm{D}}(k) = \frac{3}{k^2}(\sin(k)/k - \cos(k)). \tag{53}$$

For the one-cell case we only need to know the amplitude and scale dependence of σ_R^2 defined as

$$\sigma^2(R) = \int \frac{\mathrm{d}^3\mathbf{k}}{(2\pi)^3} P^{\mathrm{lin}}(k) W_{3\mathrm{D}}^2(kR). \tag{54}$$

To a first approximation, $\sigma^2(R)$ can be parametrized with a simple power law $\sigma^2(R) \sim R^{-(n_s+3)}$. It is this functional form which was used in the previous section. The detailed predictions of the PDF depend however on the precise scale dependence of $\sigma^2(R)$. Such scale dependence can be computed numerically from the shape of the power spectrum but then makes it difficult to derive the function $\varphi(\lambda)$ from the Legendre transform. So in order to retain simple analytic expressions for the whole cumulant generating function, we adopt a simple prescription for the scale dependence of $\sigma^2(R)$ given by

$$\sigma^2(R) = \frac{2\sigma^2(R_p)}{(R/R_p)^{n_1+3} + (R/R_p)^{n_2+3}}, \tag{55}$$

where R_p is a pivot scale. Such a parametrization ensures that the single-point $\Psi(\rho)$ function takes a simple *analytic* form as it involves the inverse of $\sigma^2(R)$. Note that our ansatz can be extended to an arbitrary (finite) number of terms in the denominator.

The values of the three parameters, $\sigma^2(R_p)$, n_1 and n_2 are then adjusted so that the model reproduces (i) the *measured* variance $\sigma^2(R)$, (ii) the linear theory index

$$n(R) = -3 - \frac{\mathrm{d}\log(\sigma(R))}{\mathrm{d}\log R}, \tag{56}$$

and (iii) its running parameter

$$\alpha(R) = \frac{\mathrm{d}\log(n(R))}{\mathrm{d}\log R}, \tag{57}$$

at the chosen filtering scale. It is important to point out that we do not take the amplitude of $\sigma^2(R)$ as predicted by linear theory. We consider instead its overall amplitude as a free parameter and $\sigma^2(R)$ is directly measured from the N-body results. The reason is that using the predicted value of $\sigma^2(R)$ would simply introduce too large errors and this dependence can always be scaled out using the relation of Sec. II D [58].

In Fig. 3, we explicitly show the comparison between our predictions following the prescription we just described to measured PDFs. The predictions show a remarkable agreement with the measured PDF. Recall that only one parameter, σ_R, is adjusted to the numerical data. In particular the predictions reproduce with an extremely good accuracy the PDF tails in both the low density and high density regions. The plot of the residuals shows the predictions are at the percent level over a large range of density values. And this result is obtained for a squared variance close to 0.5.

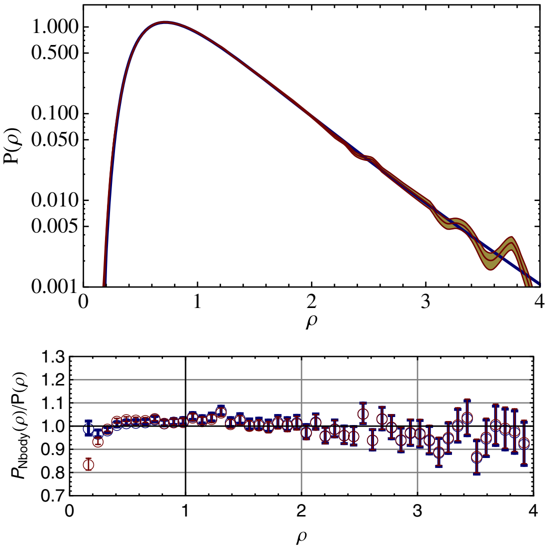

FIG. 3 (color online). Comparison with simulations (top panel) with residuals (bottom panel). The solid line is the theoretical prediction computed for a variance of $\sigma_R^2 = 0.47$ as measured in the simulation, a power law index of $n = -1.576$ and a running parameter $\alpha = 0.439$ corresponding to the input linear power spectrum. The measured PDF in the simulation is shown as a band corresponding to its 1–σ error bar (but different data points are correlated). The residuals show the ratio of the measured PDF in bins with the predictions (computed in bins as well). The thin red symbols show the comparison when the running parameter is set to zero in the prediction.

More extended comparisons with numerical simulations are shown on Fig. 15 which qualifies in more detail the validity regime of our predictions. Note that up to $\sigma = 0.64$ ($\sigma^2 = 0.41$), we see no significant departure from the results of the simulation in the whole range of available densities, that is in particular up to about the 5σ rare event in the high density tail. This success is to be contrasted with the Edgeworth expansion approach which breaks for $|\delta| \geq \sigma$ (see for instance [59]).

We observe that departures from our calculations start to be significant, of the order of 10%, when $\sigma^2(R)$ is of the order of 0.7 or more [60]. These results also show that taking into account the scale dependence of the local index through the introduction of the running parameter improves upon the predictions in the low density region. This aspect is examined in more detail in Fig. 4 which shows the ratio of the predicted PDFs with and without taking into account the running parameter. We see that the PDFs are mostly affected on their tails. This is related to the fact that the kurtosis is the lowest order cumulant to be changed when one introduces a running parameter [24], as can be verified

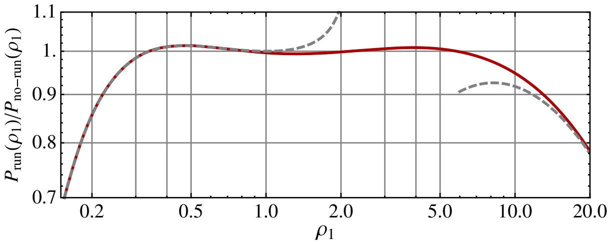

FIG. 4 (color online). Ratio of the one-point density PDF when the running parameter is taken into account over the PDF when it is not. The running model is the same as in the previous plot. The dashed lines are the ratio of the corresponding asymptotic forms in the low and high density regions.

from the relation (12). The effect is actually detectable in the low density region only and confirms the fact that the introduction of a running parameter can have a noticeable impact when comparisons at the percent level are to be done.

IV. THE STATISTICAL PROPERTIES OF THE DENSITY SLOPE AND PROFILE

We now move to the application of the general formalism to the two-cell case. Such situations have already been encountered in [26] to compute effective bias properties, and in [28] to compute the aperture mass statistics out of two concentric angular cells of fixed radius ratio. But all these applications eventually reduce to an effective one-cell case. We are interested here in genuine two-cell statistics.

Let us first make a remark that may seem trivial. Indeed, from the very definition of cumulant generating functions, one should have

$$\varphi_{2-\mathrm{cell}}(\lambda_1,\lambda_2=0)=\varphi_{1-\mathrm{cell}}(\lambda_1), \tag{58}$$

where $\varphi_{2-\mathrm{cell}}(\lambda_1,\lambda_2)$ is the cumulant generating function for cells of radii R_1 and R_2 and $\varphi_{1-\mathrm{cell}}(\lambda_1)$ is the cumulant generating function for one cell of radius R_1. Checking that the relations (23)–(28) verify this property makes a sound mathematical exercise. More generally one can show that our formulation is consistent with radii decimation, that is when one computes the cumulant generating functions of a restricted number of variables out of a larger number one gets a consistent result. The demonstration of this property is given in Appendix A.

The purpose of this section is now to define the statistical properties of the density profile, while relying on the fact that the function $\varphi(\lambda_1,\lambda_2)$ has a well-defined, but nontrivial limit, when one sets $\Delta R=R_2-R_1\ll R_1$.

A. The density slope

From the densities in two concentric cells, it is indeed always possible to define the corresponding density slope as

$$\hat{s}(R_1,R_2)=\frac{R_1}{\Delta R}[\hat{\rho}_2-\hat{\rho}_1]. \tag{59}$$

In the limit of a vanishing smoothing radius difference, $\hat{s}$ will define the local density slope. In the following we will in particular see that this is a genuine limit in the sense that it leads to regular and nontrivial expressions.

Let us start with basic preliminary calculations; to avoid too complicated notations, let us define

$$\sigma^2_{R_1}\equiv\sigma^2(R_1,R_1), \tag{60}$$

$$\sigma^2_{R_1R_2}\equiv\sigma^2(R_1,R_2), \tag{61}$$

$$\sigma^2_{R_2}\equiv\sigma^2(R_2,R_2), \tag{62}$$

which are quantities involved in the expressions of cumulants. The variance of $\hat{s}$ is then for instance given by

$$\langle\hat{s}^2\rangle=\left(\frac{R_1}{\Delta R}\right)^2(\sigma^2_{R_1}-2\sigma^2_{R_1R_2}+\sigma^2_{R_2}). \tag{63}$$

From the general theory, Eqs. (23)–(28) implemented for two cells, one can compute the generating function of joint density contrasts in concentric cells [61] in the limit of small λ_i. Up to third order it is explicitly given by

$$\begin{aligned}\varphi(\lambda_1,\lambda_2)={}&\lambda_1+\lambda_2+\frac{1}{2}\lambda_1^2\sigma^2_{R_1}+\frac{1}{2}\lambda_2^2\sigma^2_{R_2}+\lambda_1\lambda_2\sigma^2_{R_1R_2}+\lambda_1^3\left(\frac{1}{2}\nu_2\sigma^4_{R_1}+\frac{1}{6}R_1\sigma^2_{R_1}\frac{\mathrm{d}}{\mathrm{d}R_1}\sigma^2_{R_1}\right)+\lambda_2^3\left(\frac{1}{2}\nu_2\sigma^4_{R_2}+\frac{1}{6}R_2\sigma^2_{R_2}\frac{\mathrm{d}}{\mathrm{d}R_2}\sigma^2_{R_2}\right)\\&+\lambda_1^2\lambda_2\left(\frac{1}{2}\nu_2\sigma^2_{R_1R_2}(\sigma^2_{R_1,R_2}+2\sigma^2_{R_1})+\frac{1}{6}\left(2R_1\sigma^2_{R_1}\frac{\partial}{\partial R_1}\sigma^2_{R_1R_2}+\sigma^2_{R_1R_2}\left(2R_2\frac{\partial}{\partial R_2}\sigma^2_{R_1R_2}+R_1\frac{\mathrm{d}}{\mathrm{d}R_1}\sigma^2_{R_1}\right)\right)\right)\right)\\&+\lambda_1\lambda_2^2\left(\frac{1}{2}\nu_2\sigma^2_{R_1R_2}(\sigma^2_{R_1R_2}+2\sigma^2_{R_2})+\frac{1}{6}\left(2R_2\sigma^2_{R_2}\frac{\partial}{\partial R_2}\sigma^2_{R_1R_2}+\sigma^2_{R_1R_2}\left\{2R_1\frac{\partial}{\partial R_1}\sigma^2_{R_1R_2}+R_2\frac{\mathrm{d}}{\mathrm{d}R_2}\sigma^2_{R_2}\right\}\right)\right),\end{aligned} \tag{64}$$

where $\nu_2=34/21$ for a 3D dynamics in an Einstein–de Sitter background. In Eq. (64), the cumulants and joint cumulants can be read out using definition (4) or via differentiation. For instance,

$$\langle \hat\rho_1^3\rangle_c = 3\nu_2\sigma^4_{R_1} + \sigma^2_{R_1}\frac{R_1 \mathrm{d}}{\mathrm{d}R_1}\sigma^2_{R_1}, \tag{65}$$

$$\langle \hat\rho_1^2\hat\rho_2\rangle_c = \nu_2\sigma^2_{R_1R_2}(\sigma^2_{R_1R_2} + 2\sigma^2_{R_1}) + \frac{2}{3}\sigma^2_{R_1}\frac{R_1\partial}{\partial R_1}\sigma^2_{R_1R_2} + \frac{1}{3}\sigma^2_{R_1R_2}\left(2\frac{R_2\partial}{\partial R_2}\sigma^2_{R_1R_2} + \frac{R_1 \mathrm{d}}{\mathrm{d}R_1}\sigma^2_{R_1}\right), \tag{66}$$

and the cumulants $\langle\rho_1\rho_2^2\rangle_c$ and $\langle\rho_2^3\rangle_c$ can be obtained exchanging the role of R_1 and R_2. It is then also possible to derive the explicit form for a number of auto- and cross-cumulants between the density $\hat\rho \equiv \hat\rho_1$ in the first cell and the slope $\hat s$ as defined in (59). For instance,

$$\langle \hat\rho^2\hat s\rangle_c = \frac{R_1}{\Delta R}[\langle\hat\rho_1^2\hat\rho_2\rangle_c - \langle\hat\rho_1^3\rangle_c], \tag{67}$$

$$\langle \hat\rho\hat s^2\rangle_c = \left[\frac{R_1}{\Delta R}\right]^2[\langle\hat\rho_1\hat\rho_2^2\rangle_c - 2\langle\hat\rho_1^2\hat\rho_2\rangle_c + \langle\hat\rho_1^3\rangle_c], \tag{68}$$

$$\langle \hat s^3\rangle_c = \left[\frac{R_1}{\Delta R}\right]^3[\langle\hat\rho_2^3\rangle_c - 3\langle\hat\rho_1\hat\rho_2^2\rangle_c + 3\langle\hat\rho_1^2\hat\rho_2\rangle_c - \langle\hat\rho_1^3\rangle_c]. \tag{69}$$

Following the one-cell case (see for instance [6]) it is possible to formally define the reduced cross-correlations that are independent on the overall amplitude of the power spectrum. More precisely, the reduced cross-correlations can be defined as

$$S_{p0} = \frac{\langle\hat\rho^p\rangle_c}{\langle\hat\rho^2\rangle_c^{p-1}}, \tag{70}$$

$$S_{pq} = \frac{\langle\hat\rho^p\hat s^q\rangle_c}{\langle\hat\rho^2\rangle_c^{p-1}\langle\hat\rho\,\hat s\rangle_c\langle\hat s^2\rangle_c^{q-1}}, \tag{71}$$

$$S_{0q} = \frac{\langle\hat s^q\rangle_c}{\langle\hat s^2\rangle_c^{q-1}}. \tag{72}$$

From the previous expressions these quantities can be computed in the limit of an infinitely small variance.

B. Cumulants and slope in the limit $(\Delta R)/R \to 0$

Let us now consider the statistical properties of $\hat s$ in the limit $(\Delta R)/R \to 0$. To start with, let us compute the variance of the slope $\hat s$ in the limit $\Delta R/R \to 0$. Its variance is formally given by

$$\langle\hat s^2\rangle = \frac{R_1^2\partial^2}{\partial R_1\partial R_2}\sigma^2_{R_1R_2}\Big|_{R=R_1=R_2}. \tag{73}$$

This expression can easily be expressed in terms of the power spectrum,

$$\langle\hat s^2\rangle = \int\frac{\mathrm{d}^3\mathbf{k}}{(2\pi)^3}P^{\mathrm{lin}}(k)\tilde W^2_{\mathrm{3D}}(kR), \tag{74}$$

where $\tilde W_{\mathrm{3D}}(k)$ is the logarithmic derivative of $W_{\mathrm{3D}}(k)$,

$$\tilde W_{\mathrm{3D}}(k) = \frac{\mathrm{d}}{\mathrm{d}\log k}W_{\mathrm{3D}}(k), \tag{75}$$

which for the 3D case can be written,

$$\tilde W_{\mathrm{3D}}(k) = \frac{1}{k^3}[(9k\cos(k) + 3(k^2-3)\sin(k)]. \tag{76}$$

Note that for a power law spectrum of index n_s this variance is only defined when $n_s < -1$. For practical application to cosmological models that resemble the concordant model, the effective index n_s decreases to -3 at small scales and the variance of $\hat s$ is always finite. This property however suggests that the amplitude of the slope fluctuations could be dominated by density fluctuations at scales significantly smaller than the smoothing radius if the latter is large enough. This is not expected to be the case however for the filtering scales we explore in this investigation. More precisely, provided the power spectrum index is in the range $[-3,-1]$, the amplitude of the variance of $\hat s$ can be expressed in terms of the variance of the density as

$$\langle\hat s^2\rangle = \sigma_R^2\frac{n_s(n_s+3)(n_s+5)}{4(n_s+1)}. \tag{77}$$

Let us now see how the whole statistical properties of the variable $\hat s$ can be derived from our formalism. Let us first explore the consequence of the change of variable, $(\hat\rho_1,\hat\rho_2) \to (\hat\rho,\hat s)$. Instead of describing the joint PDF as a function of the associated variables λ_1 and λ_2 we can build it with the variable associated to $\hat\rho$ and $\hat s$. Noting that $\lambda_1\hat\rho_1 + \lambda_2\hat\rho_2$ can be written as

$$\lambda_1\hat\rho_1 + \lambda_2\hat\rho_2 = (\lambda_1+\lambda_2)\hat\rho_1 + \frac{\Delta R}{R_1}\lambda_2\hat s, \tag{78}$$

as a consequence, the joint cumulant generating function of $\hat\rho_1$ and $\hat s$ is given by $\varphi(\lambda_1,\lambda_2)$ when written as a function of

$$\lambda = \lambda_1 + \lambda_2, \qquad \mu = \frac{\Delta R}{R_1}\lambda_2, \tag{79}$$

which are the variables associated with the Laplace and inverse Laplace transform of $\mathcal{P}(\hat\rho_1,\hat s)$. One can also check that, following this definition, $\varphi(\lambda,\mu)$ is the Legendre transform of $\Psi(\rho_1, s = (\rho_2-\rho_1)R_1/\Delta R)$.

Let us then explore the whole statistical properties of $\hat s$ in the limit of a vanishing radius difference $(\Delta R)/R \to 0$. First note that the reduced skewness of $\hat s$ is still finite [62] and has a nontrivial value. It is given by

$$S_{03}^{\Delta R\to 0} = 2 + \left. \frac{\frac{\partial}{\partial R_1}\sigma^2_{R_1 R_2}}{\frac{R_1\partial^2}{\partial R_1 \partial R_2}\sigma^2_{R_1 R_2}} \right|_{R=R_1=R_2} (6\nu_2 - (\tilde{n}+3)), \tag{80}$$

where the effective index, $\tilde{n}$, is defined as

$$\frac{1}{\langle \hat{s}^2\rangle}\frac{\mathrm{d}}{\mathrm{d}\log R}\langle \hat{s}^2\rangle = -(\tilde{n}+3). \tag{81}$$

We will see in the following that this feature, the fact that reduced cumulants remain finite, extends to the whole generating function.

C. Analytic properties of $\varphi(\lambda,\mu)$

Let us now turn to the full analytical properties of $\varphi(\lambda,\mu)$, for a finite radius difference to start with, and then in the limit of vanishing radius difference. It is to be noted that, as for the one-cell case, not all values of λ and μ are accessible. This is due to the fact that the ρ_i –λ_i relation cannot always be inverted via Eq. (24). The boundary of the region of interest is signaled by the fact that the determinant of the transformation vanishes, i.e., $\det[\partial^2\Psi(\{\rho_k\})/\partial\rho_i\partial\rho_j] = 0$. This condition is met for finite values of both ρ_i and λ_i. The resulting critical lines are shown as thick solid lines in Fig. 5. Note that $\varphi(\lambda_1,\lambda_2)$ is also finite at this location. Within this line φ is defined; beyond this line it is not. Let us now explore the behavior of $\varphi(\lambda,\mu)$ when $\Delta R/R \to 0$. This is actually a cumbersome limit to take. One of the reasons is that the matrix Ξ_{ij} then becomes singular. More precisely the determinant of the cross-correlation function takes the form

$$\det[\Sigma_{ij}(R, R+\Delta R)] = R^{-2(3+n_s)}\left(\frac{\Delta R}{R}\right)^2 \frac{-9+n_s^2}{4(1+n_s)}$$

at leading order in $\Delta R/R$ and when $n_s < -1$. For a power law spectrum, the actual coefficients read

$$\Xi_{11}(R,\Delta R) = \frac{2(n_s+1)R^{n_s+3}}{(\frac{\Delta R}{R})^2(n_s^2-9)}\left(\left(\frac{\Delta R}{R}\right)^2(n_s^2+7n_s+12) - 2\frac{\Delta R}{R}(n_s+3)+2\right), \tag{82}$$

$$\Xi_{12}(R,\Delta R) = -\frac{R^{n_s+3}}{2(\frac{\Delta R}{R})^2(n_s^2-9)}\left(\left(\frac{\Delta R}{R}\right)^2(n_s^3+8n_s^2+23n_s+24) - 4\frac{\Delta R}{R}(n_s^2+4n_s+3)+8(n_s+1)\right), \tag{83}$$

$$\Xi_{22}(R,\Delta R) = \frac{4(n_s+1)R^{n_s+3}}{(\frac{\Delta R}{R})^2(n_s^2-9)}. \tag{84}$$

All these coefficients are diverging like $(R/\Delta R)^2$. What we need to compute is however $\Psi(\rho,s)$ for finite values of ρ and s. In this case ρ_2 is also infinitely close to ρ_1 with $\rho_2 - \rho_1 = s\Delta R/R$ with a fixed value for s. Then the resulting value of $\Psi(\rho,s)$ is finite in the limit $\Delta R \to 0$. Assuming the form (13) for $\zeta(\tau)$ one gets

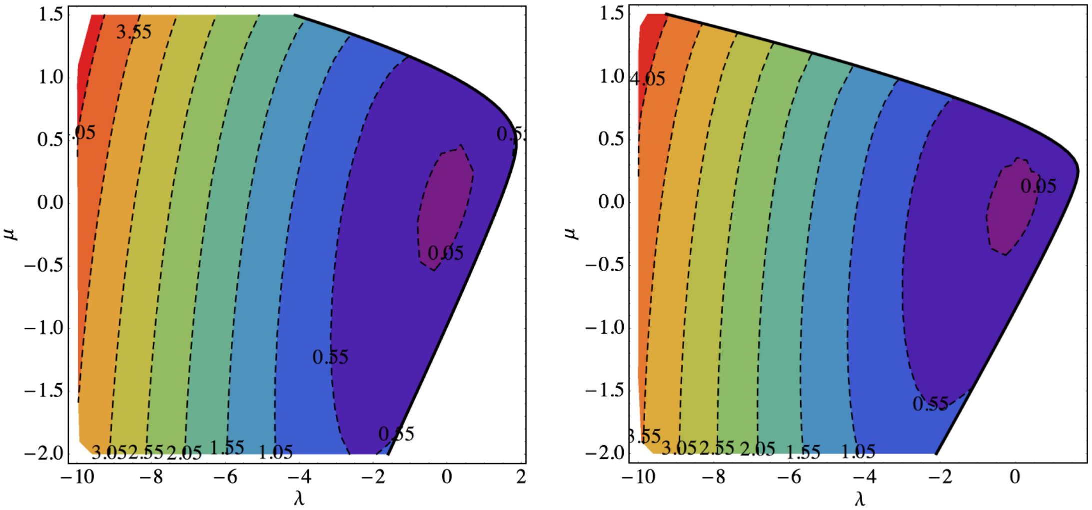

FIG. 5 (color online). Contour plot of $\varphi(\lambda,\mu)-\lambda$ (left panel) with a finite radius difference $\Delta R/R = 1/10$ and (right panel) with $\Delta R/R \to 0$. We see that the structure of the critical region, although deformed, is preserved. In both cases, the restriction of $\varphi(\lambda,\mu)$ to $\mu = 0$ is precisely the one-cell cumulant generating function considered in Sec. III.

$$\Psi(\rho,s)=\frac{R^{3+n_s}\rho^{n_s/3+(\nu-2)/\nu}}{2(n_s^2-9)(s+3\rho)^2}\{s^2[\nu^2n_s^3(\rho^{\frac{1}{\nu}}-1)^2+3n_s(5\nu^2(\rho^{\frac{1}{\nu}}-1)^2+16\nu(\rho^{\frac{1}{\nu}}-1)+12)$$
$$+4\nu n_s^2(\rho^{\frac{1}{\nu}}-1)(2\nu(\rho^{\frac{1}{\nu}}-1)+3)+36(\nu(\rho^{\frac{1}{\nu}}-1)+1)]+9\nu^2\rho^2n_s(n_s^2+8n_s+15)(\rho^{\frac{1}{\nu}}-1)^2$$
$$+6s\nu\rho(n_s+3)(\rho^{\frac{1}{\nu}}-1)(\nu n_s^2(\rho^{\frac{1}{\nu}}-1)+n_s(5\nu(\rho^{\frac{1}{\nu}}-1)+6)+6)\}. \tag{85}$$

The function $\varphi(\lambda,\mu)$ can then be obtained by Legendre transform. Like for the one-cell case, the transformation becomes critical when the inversion of the stationary condition is singular. For the new variables, it is also occurring when the determinant of the second derivatives of Ψ vanishes,

$$\det\left[\frac{\partial^2\Psi(\rho,s)}{\partial\rho\partial s}\right]=0, \tag{86}$$

which generalizes the condition (42). This condition defines the location of the critical line which can then be visualized in the $\lambda-\mu$ plane (thick lines in Fig. 5). Note that the no-shell crossing condition, which in this limit reads $s>-3\rho$, is located beyond this critical line and is therefore not relevant.

In the regular region, the contour lines of $\varphi(\lambda,\mu)$ are shown in Fig. 5 for both a finite ratio $\Delta R/R$ and when it is infinitely small. This figure explicitly shows in particular that the limit $\Delta R\to 0$ is nonpathological, in the sense that the location of the critical line and the actual value of the cumulant generating function converge to well-defined values in that limit. The convergence is however not very rapid and in practice we will use finite differences for comparisons with simulations.

Finally, to conclude this subsection we also compare these contour plots with those measured in simulations. There, one actually computes the explicit sum

$$\exp[\varphi(\lambda,\mu)]=\frac{1}{N_x}\sum_x\exp(\lambda\hat{\rho}_x+\mu\hat{s}_x), \tag{87}$$

where $\hat{\rho}_x$ and $\hat{s}_x$ are the measured values of $\hat{\rho}$ and $\hat{s}$ in a cell centered on x (in practice on grid points) and N_x is the number of points used (see Appendix D for details). Then $\varphi(\lambda,\mu)$ is always well defined, irrespective of the values of λ and μ. To detect the location of a critical line one should then rely on the properties it is associated with. From the analysis of the one-cell case it appears that for $\lambda>\lambda_c$, $\varphi(\lambda)$ is ill defined because $\int\mathcal{P}(\hat{\rho})\exp(\lambda\hat{\rho})d\hat{\rho}$ diverges. More precisely when $\lambda\to\lambda_c$ the value of $\varphi(\lambda)$ becomes dominated by the rare event tail. It makes such a quantity very sensitive to cosmic variance and in practice the critical line position is therefore associated with a diverging cosmic variance. In the two-cell case, we encounter the same effects. To locate we therefore simply cut out part of the $(\lambda-\mu)$ plane for which the measured variance of $\varphi(\lambda,\mu)$ exceeds a significant fraction of its measured value. We set this fraction to be 20% [63]. This criterium give rises to the solid line shown in Fig. 6. This figure is now to be compared to the left panel of Fig. 5. Although the figures are not identical they clearly exhibit the same patterns.

D. Slope cumulant generating function and PDF

When one wishes to build the PDF of $\hat{s}$, one needs to restrict $\varphi(\lambda,\mu)$ presented in the previous section to the $\lambda=0$ axis, i.e. focus on $\varphi_s(\mu)\equiv\varphi(\lambda=0,\mu)$. Figure 6 shows that $\varphi_s(\mu)$ has two extrema points, one corresponding to a positive value of μ, μ_c^+, and one to a negative value μ_c^-. The resulting global shape of $\varphi_s(\mu)$ is shown in Fig. 7, where it is also compared to the results where $\Delta R/R$ is kept finite. It actually shows that the limit $\Delta R/R$ is genuine at the level of the cumulant generating function but is reached for very small values of $\Delta R/R$. When predictions are compared with simulations for which the slope is measured with finite differences, it is necessary to use a finite difference ΔR.

We are now in position to build the one-point PDF of the density slope via the inverse Laplace transform of the cumulant generating function. It should be clear from the singular behavior of $\varphi_s(\mu)$ that it will exhibit exponential cutoffs on both sides, for positive and negative values of $\hat{s}$ although not *a priori* in a symmetric way. In practice, to do the complex plane integration, we build the function $\varphi_s(\mu)$ for the actual power spectrum of interest, and *then* build an

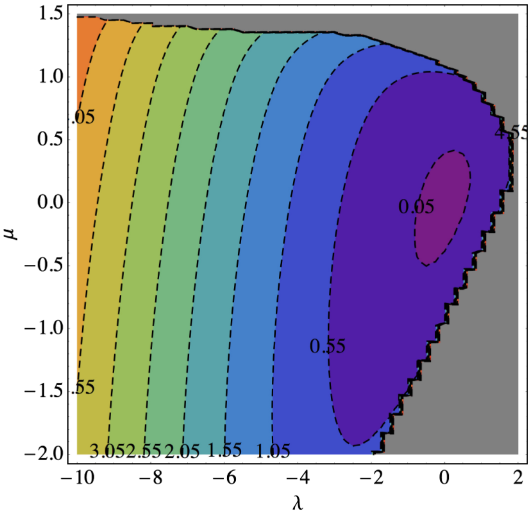

FIG. 6 (color online). Contour plot of $\varphi(\lambda,\mu)-\lambda$, from the simulation. It is to be compared with the left panel of Fig. 5.

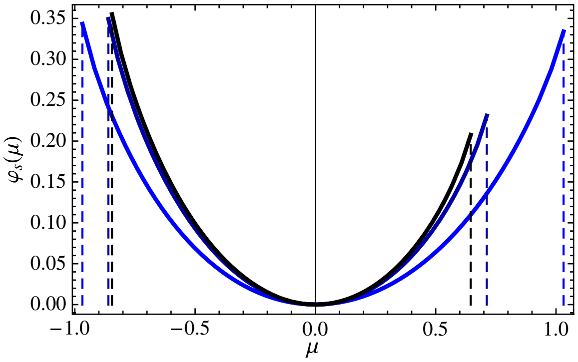

FIG. 7 (color online). The slope generating function $\varphi_s(\mu)$ for finite differences $\Delta R/R = 0.1$ and $\Delta R/R = 0.01$, and in the limit $\Delta R/R \to 0$. The corresponding curves are respectively in blue, darker blue and black. The vertical dashed lines show the locations of the critical points, μ_c^- and μ_c^+.

effective form $\zeta_{\rm eff}(\tau)$ that reproduces the numerical integration following Eqs. (38)–(39) as explained in [28]. In practice we use a seventh order polynomial to do the fit. We then proceed via integration in the complex plane using the usual approach (see Appendix B). The results for $R = 10h^{-1}$ Mpc and $z = 1.46$ and $z = 0.97$ is presented in the top panel of Fig. 8. The figure clearly exhibits the expected double cutoffs. Discrepancies between numerical results and theory that can be seen in the bottom panels for $\hat{s} \approx -0.5$ are not clearly understood (cosmic variance, numerical artifacts?).

E. The expected constrained slope and profile

Let us finally move to the key result of this paper. In the previous subsection we built the marginal PDF of $\hat{s}$; we now focus on the conditional properties of $\hat{s}$ given $\hat{\rho}_1 = \hat{\rho}(<R_1)$ at a given $R = R_1$, whether $\hat{s}$ is defined from a nearby radius of not. Mathematically it can be expressed in terms of the joint PDF, $\mathcal{P}(\hat{\rho}_1, \hat{\rho}_2)$, as

$$\langle \hat{s} \rangle_{\hat{\rho}_1} = -\frac{R}{\Delta R}\hat{\rho}_1 + \frac{R}{\Delta R \mathcal{P}(\hat{\rho}_1)} \int \mathrm{d}\hat{\rho}_2 \hat{\rho}_2 \mathcal{P}(\hat{\rho}_1, \hat{\rho}_2), \quad (88)$$

given that

$$\int \mathrm{d}\hat{\rho}_2 \hat{\rho}_2 \mathcal{P}(\hat{\rho}_1, \hat{\rho}_2) = \int_{-i\infty}^{+i\infty} \frac{\mathrm{d}\lambda_1}{2\pi i} \frac{\partial \varphi(\lambda_1, \lambda_2)}{\partial \lambda_2}\bigg|_{\lambda_2=0} \exp(-\lambda_1 \hat{\rho}_1 + \varphi(\lambda_1)), \quad (89)$$

which can be obtained by explicit integration in the complex plane [64]. Note that the solution of the stationary equations, Eq. (28), yields the identity

$$\frac{\partial \varphi(\lambda_1, \lambda_2)}{\partial \lambda_2}\bigg|_{\lambda_2=0} = \rho_2(\lambda_1, \lambda_2 = 0). \quad (90)$$

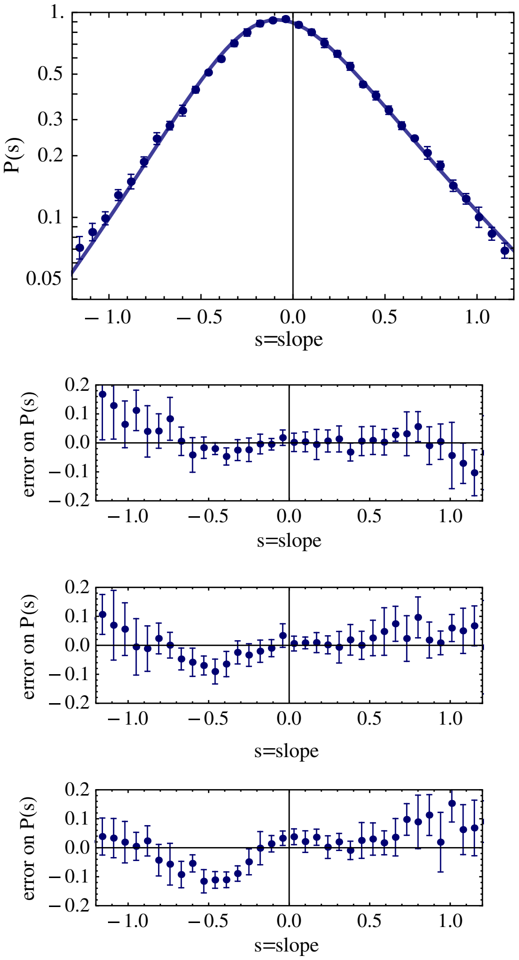

FIG. 8 (color online). The PDF of the slope for $z = 1.46$. The bottom panels show the residuals for $z = 1.46$, $z = 0.97$ and $z = 0.65$ from top to bottom.

For the saddle point solution corresponding to the low ρ regime, λ_1 and $\hat{\rho}_1$ in Eq. (89) are related through the stationary condition. In this limit we therefore have

$$\langle \hat{\rho}_2 \rangle_{\hat{\rho}_1} = \bar{\rho}_2(\hat{\rho}_1), \quad (91)$$

where $\bar{\rho}_2(\hat{\rho}_1)$ is the solution of the system

$$\lambda_1 = \frac{\partial \Psi(\rho_1, \bar{\rho}_2)}{\partial \rho_1}, \qquad 0 = \frac{\partial \Psi(\rho_1, \bar{\rho}_2)}{\partial \rho_2}. \quad (92)$$

These calculations can be extended to the constrained variance of the slope. The computation follows the same line of derivation but is slightly more involved. It is presented in Appendix C.

Let us now present the expected slope from exact complex plane numerical integration, using the analytical saddle point approximations and as measured in numerical simulations. For instance, Fig. 9 shows the expected slope given by $10. \times [\hat{\rho}(1.1R) - \hat{\rho}(R)]$ as a function of $\hat{\rho}(R)$

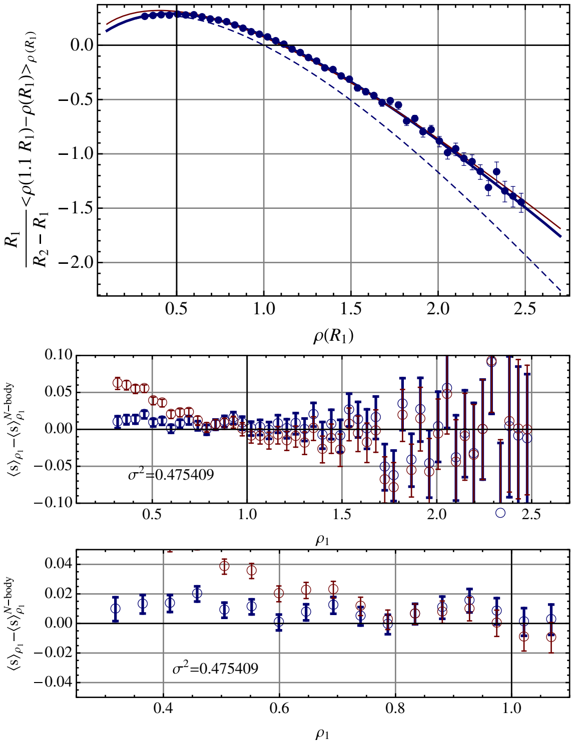

FIG. 9 (color online). (Top panel) The conditional profile, $\langle\hat{s}\rangle_{\hat{\rho}(<R_1)}$ as a function of $\hat{\rho}(<R_1)$. The thick blue solid line is the result of the numerical integration, the thin dashed line the saddle point approximation Eq. (91). We also present the power law approximation case as a thin (red) solid line. It is shown to depart from the exact prediction in the low density region. The agreement between the theory and the measurements near the origin is quite remarkable. The bottom panels show the residuals computed in bins as a function of the density (with a zoomed plot below). Again the thick symbols correspond to the exact calculation, the thin symbols correspond to the power law approximation.

using the same cosmological parameters as for Fig. 2. The solid lines are the results of complex plane integrations and the dashed line is the saddle point approximation. The latter is found to perform very poorly when compared to simulation. We note also that the low density part of the prediction can only be accounted for when the running parameter is taken into account. This is clearly visible in the middle and bottom panels when one compares the (thick) blue and the (thin) red marks. These comparisons show that the analytical predictions are accurate at percent level in a large range of parameters.

Let us finally turn to the more global properties of the density in cells and consider the density *profile* defined as the constrained density $\hat{\rho}(R_2)$ given $\hat{\rho}(R_1)$ as a function of R_2. Technically computing expected profiles or slopes is equivalent. The second point of view allows however to visualize what should be the radial variation of the density profile, and its fluctuations, of an underdense or an overdense region. The result of such a calculation is presented in Fig. 10 which shows the expected density as a function of the radius R_2 and for various values of $\hat{\rho}(R_1)$. In the same plot we also show the expected 1-σ variance about the expectation values. Both quantities are computed using the exact complex plane integration and compared to their saddle point approximation counterparts. The difference is only significant for $\hat{\rho}(R_1)=1.25$. Interestingly for low density prior, e.g. $\hat{\rho}(R_1)=0.2$ in the figure, the variance is small (and significantly smaller than the variance of $\hat{s}$ in the absence of prior on the density). That implies that all voids should look similar, probably a good starting point for exploring the statistical properties of the field while focussing on these regions.

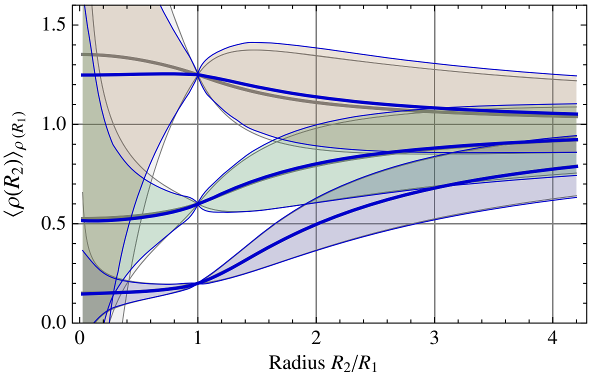

FIG. 10 (color online). The conditional profile as a function of R_2 and for different choices of $\hat{\rho}(R_1)$ [to which $\hat{\rho}(R_2)$ is equal to at $R_2=R_1$]. The blue thick solid lines are the results of numerical integrations; the colored thin lines show the 1-σ variance about the expectation. The close-by gray lines are the same calculations but using the saddle point approximations of Eqs. (91) and (C5) respectively. Note in particular the smaller variance of the underdense profile near $R_2\sim 0$.

Comparisons of the latter prediction with numerical simulations is made in Fig. 11 where we give both the measurements of the expected profile and their variance for a given constraint. The only difference with the theoretical predictions is that the constraints are binned, i.e. the prior is that the density ρ_1 is assigned in a given bin of width 0.2 centered on the values 0.35,0.74,1.13,1.52,1.92. As the theoretical predictions do not take into account the binning, there is a noticeable departure between the predicted variance and its measured value near $R_2/R_1\approx 1$ due to the width of the bin. But, this departure notwithstanding, the agreement between the theoretical predictions and the measured quantities, for both the expected profile and its variance, is just striking. Only when the constraint density is large (top two panels) can we see some slight departure of the variances with the theory for small radii, which is due to the fact that they correspond to regions entering the nonlinear regime.

F. Joint *n*-cells PDF

The results presented in the previous section give us confidence in the general framework we have adopted here.

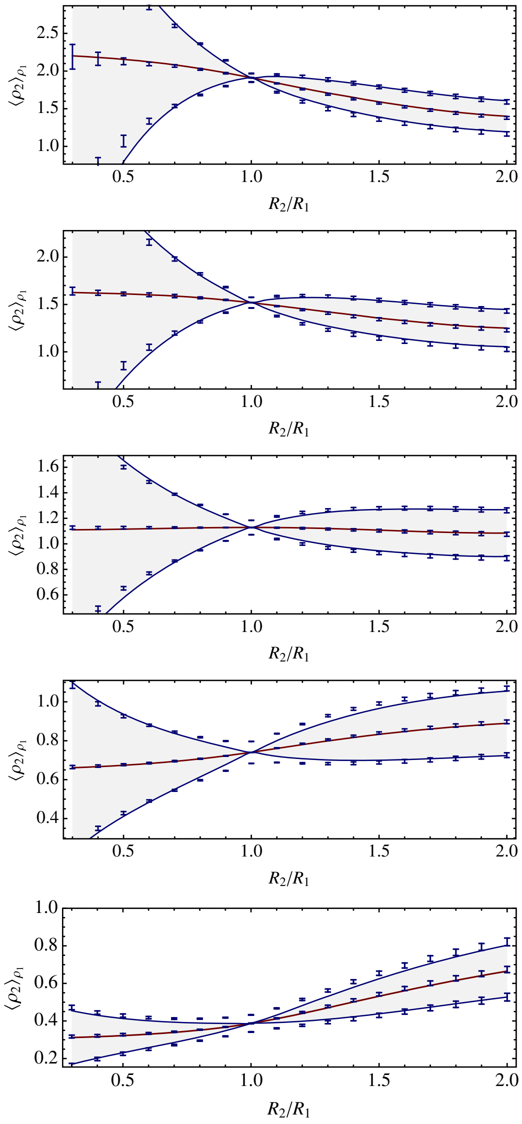

FIG. 11 (color online). Same quantities as in Fig. 10 measured here in simulations. The solid lines are the theoretical predictions and the points with error bars are the measurements for both the expected value and its variance. The agreement is spectacular in particular for low density constraints.

It has to be stressed that all of the properties we have described are simultaneously captured with the shape of the multiple cell cumulant generating function, $\varphi(\{\lambda_k\})$, or its counterpart, the n-cell PDF, $\mathcal{P}(\{\hat{\rho}_k\})$. We should keep in mind that we could have considered the former only to compare with simulations but we dramatically lack intuition for such a representation. By contrast we have much better intuition of what n-cell PDFs are. So far we have considered only the one-cell PDF. In the following we succinctly consider the derivation of the multicell PDF in our framework.

Hence let us consider a set of n concentric cells and its cumulant generating function $\varphi(\{\lambda_k\})$. In principle the corresponding PDF, $\mathcal{P}(\{\hat{\rho}_k\})$, is to be obtained from inverse Laplace transform. Such a computation appears extremely challenging to implement and we have not succeeded yet in producing a full two-cell PDF. We can however present its low density approximation, the counterpart of Eq. (46), for a multidimensional case. It is based on the use of the saddle point approximation of Eq. (40) assuming the overall variance is small. It leads to a similar condition that should be met at the saddle point $\{\lambda_s\}_i$,

$$\frac{\partial}{\partial\lambda_k}\Big[\sum_i \lambda_i\hat{\rho}_i - \varphi(\{\lambda_i\})\Big] = 0, \tag{93}$$

which leads to

$$\hat{\rho}_i = \rho_i(\{\lambda_k\}), \tag{94}$$

and with the constraint that

$$\det\left[\frac{\partial^2\Psi}{\partial\rho_k\partial\rho_l}\right] > 0 \tag{95}$$

at the saddle point position. The resulting expression for the density PDF generalizes Eq. (46) to

$$\mathcal{P}(\{\hat{\rho}_k\}) = \frac{1}{(2\pi)^{n/2}}\sqrt{\det\left[\frac{\partial^2\Psi}{\partial\hat{\rho}_k\partial\hat{\rho}_l}\right]}\exp\left[-\Psi(\{\hat{\rho}_k\})\right]. \tag{96}$$

This analytic expression is expected to be an approximate form for the exact PDF in underdense regions.

We suggest that in the absence of computable multiple cell PDFs, this form could be used, provided one makes sure to restrict its application to its proper region of validity. It is interesting to note that, in this framework, the *parameter dependence* of the mode of that PDF and its local curvature tensor can be straightforwardly computed from it analytically. In the concluding section we will simply sketch a way to constrain key cosmological parameters using this form.

V. CONCLUSIONS AND PROSPECTS

A. Summary

In the context of upcoming large wide field surveys we revisited the derivation of the cumulant generating functions of densities in spherical concentric cells in the limit of a vanishing variance and we conjectured that it correctly represents the generating function for finite values of the variance. We noted that such a quantity is an observable in itself and could probably be used as a cosmological indicator. In this study we however focused our efforts on its counterpart, the multicell density PDF.

We first computed the resulting one-cell density PDF. These results were tested with unprecedented accuracy, in particular taking into account the scale variation of the power spectrum index. Comparisons to modern N-body simulations showed that predictions reach percent order accuracy (when the density variance is measured from simulations) for a large range of density values, as long as the variance is small enough. It confirmed in particular that this formalism gives a good account of the rare event tails: predictions are in agreement with the numerical measurements down to numerical precision.

We took advantage of the finite variance generating function formalism to explore its implications to the two-cell case in a novel regime. In particular we derived the statistical properties of the local density slope, defined as the infinitesimal difference of the density in two concentric cells of (possibly infinitesimally) close radii. We gave its mean expectation, and its expectation constrained to a given density. From the properties of the local slope, one can also construct the overall expected profile, i.e. the density as a function of the radius, and its fluctuations. We found the latter to be of particular interest when focusing on voids, as in these regions, the variances around the mean profile are significantly reduced (though the relative fluctuations less so). In particular we suggest below a possible method to constrain cosmological and gravity models from these low density regions. All these predictions were successfully compared to simulations.

B. Prospects

The full statistical power of the approach presented in this paper would ultimately be encoded in the shape of the two-cell density PDF but we do not know at this stage how to properly invert the exact expression given by Eq. (40) in this two-cell regime. Despite this limitation, as we do not have simulations that span different gravity models, let us use the saddle point form of Eq. (96) assuming it is exact (hence avoiding the issue of the domain of validity of that analytic fit to the exact PDF), and use its dependence on key (cosmic) parameters to infer the precision with which cosmological parameters could be constrained.

Focusing the analysis on two quantities, the parameter ν that encodes the spherical collapse dynamics [see Eq. (13)] and the power law index n_s, let us simply consider sets of about 2 000 and 11 000 independent measurements drawn in concentric spheres of radii 10 and 11 Mpc$/h$ and such that $0.05 < \rho_1 < 0.5$ and $-0.02 < \Delta\rho/\rho_1 < 0.06$ (i.e. near the peak of the PDF). The samples are drawn directly from the two-cell PDF for chosen values of the power law power spectrum and ν parameter starting respectively with $n_s = -2.5$ and $\nu = 3/2$. The likelihood of the models where n_s and ν vary in the range $[-0.12, 0.12]$ around the reference value is computed.

The resulting mean (over 25 independent samples) log likelihood of the data set as a function of $\Delta\nu/\nu$ and $\Delta n_s/n_s$ is displayed in Fig. 12 (at one, three and five sigma respectively) [65]. As expected, the likelihood contours are centered on the zero offset values; they yield the precision that could be reached in a survey of a useful volume of about $(200h^{-1}\ \mathrm{Mpc})^3$ (red contours) and $(360h^{-1}\ \mathrm{Mpc})^3$ (blue contours). These sample sizes are not unreasonable. Indeed, the volume span with about 30 000 spheres corresponds to the volume covered by the simulation and we found that, in doing so, the error bars on relevant quantities such as profiles (as shown in Fig. 9) were of the same order as the one measured in the simulation we used throughout the paper. At face value, relative accuracies below the percent on (n_s, ν) could be reached with such surveys. Yet, this numerical experiment is, at this stage, at best illustrative. We are indeed aware that in more realistic situations, one would have to properly account for the domain of validity of the above functional form, which would take us beyond the scope of this paper. Another open question would be to estimate how many concentric cells should be used to get an optimal constraint for a given set of cosmic parameters, but the answer to this question will probably depend on the geometry of the available survey.

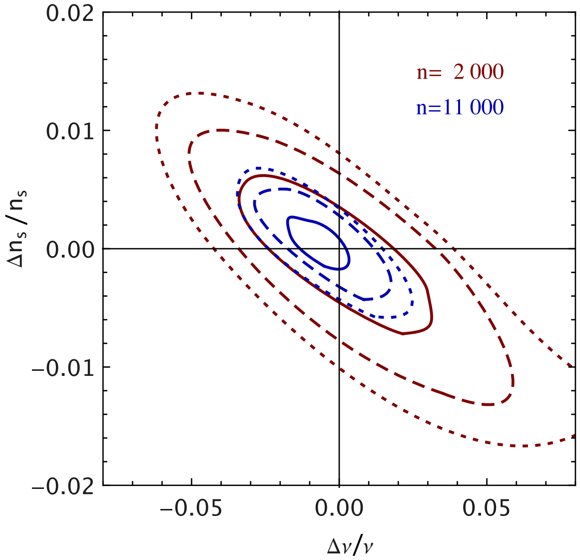

FIG. 12 (color online). The likelihood contours at one, three and five sigmas around the reference model ($n_s = -2.5$, $\nu = 3/2$), drawn from ~11 000 measurements (inner blue contours) and ~2 000 measurements (outer red contours) of the densities in concentric shells of radii 10 and 11 Mpc$/h$.

Should these problems be alleviated, effective implementation of such cosmological tests would still be far fetched. In particular galaxy catalogs in z space break the local spherical symmetry in a complex way making the application of such a method impractical. One way to avoid this problem is to stick to observations for which this method is applicable, such as *projected* densities along the line of sight. It can be done either in the context of cosmic shear observations or for photometriclike redshift surveys. In both cases the point is not to reconstruct the spherical 3D statistics but the circular two-dimensional statistics for which the whole method should be applicable following early investigations in [27,28]. The accuracy of the predictions still has to be assessed in this context. Another missing piece that can be incorporated is the large distance correlation of statistical indicators such as profiles and constrained profiles. Following [27] it is indeed within reach of this formalism to compute such quantities. We would then have a fully working theory that could be exploited in real data sets.

ACKNOWLEDGMENTS

We warmly thank D. Pogosyan for triggering our interest in studying the statistics of void regions. We also thank him for his many comments. This work is partially supported by Grants No. ANR-12-BS05-0002 and No. ANR-13-BS05-0005 of the French Agence Nationale de la Recherche and by the National Science Foundation under Grant No. NSF PHY11-25915. The simulations were run on the HORIZON cluster. C. P. thanks KITP and the University of Cambridge for their hospitality while this work was completed. We acknowledge support from S. Rouberol for running the cluster for us.

APPENDIX A: RADII DECIMATIONS

The purpose of this appendix is to make sure that the expression of $\varphi(\{\lambda\})$ is consistent with variable decimation, i.e. we want to make sure that

$$\varphi(\{\lambda_1,\ldots,\lambda_n\}) \\ = \varphi(\{\lambda_1,\ldots,\lambda_n,\lambda_{n+1}=0,\ldots,\lambda_{n+m}=0\}), \qquad (A1)$$

where the left-hand side is computed from n cells whereas the right-hand side is computed with $n+m$ cells.

In order to prove this property, let us define a set $\mathcal{A}$ of n cells and a set $\mathcal{B}$ of m cells. One can then define the covariance matrix $\sigma_{ij}(\rho_i,\rho_j)$ as in (17) between two any cells of the union of $\mathcal{A}$ and $\mathcal{B}$.

We first need to establish a preliminary relation between the element of the inverse matrix $\Xi_{ij}(\{\rho_k\})$ and the covariance matrix. From

$$\sum_{l=1}^{n}\sigma_{il}(\rho_i,\rho_l)\Xi_{lj}(\{\rho_k\}) = \delta_{ij}, \qquad (A2)$$

we indeed can derive the following relation,

$$\sigma_{il}(\rho_i,\rho_l)\frac{\partial}{\partial\rho_k}[\Xi_{lj}(\{\rho_k\})]\sigma_{jm}(\rho_j,\rho_m) \\ +\frac{\partial}{\partial\rho_k}[\sigma_{im}(\rho_i,\rho_m)] = 0, \qquad (A3)$$

where all the repeated indices run from 1 to $n+m$. One can also write this relation when the inverse matrix is defined

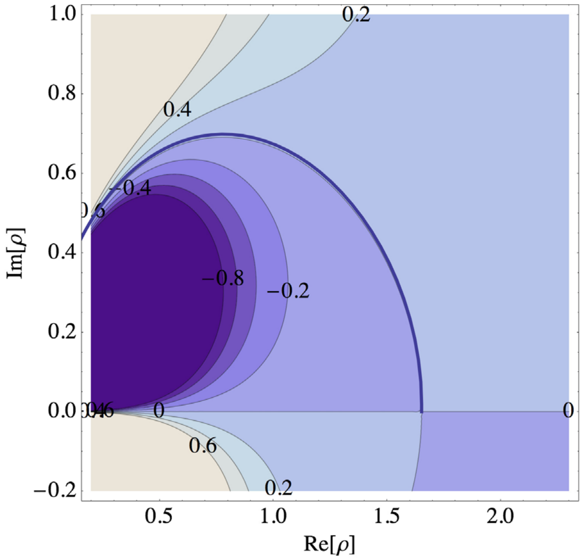

FIG. 13 (color online). The path line in the ρ complex plane. We superimposed the contour plot of the imaginary part of $\varphi(\lambda)-\lambda\hat{\rho}$ to check that it follows a $\Im[\varphi(\lambda)-\lambda\hat{\rho}]=0$ line. The starting point on the real axis correspond to the saddle point value.

from the covariance matrix of the cells restricted in $\mathcal{A}$ only. Let us define by $\hat{\Xi}_{\mu\nu}(\{\rho_{\rho\mu}\})$ this matrix and in the following restrict the Greek indices from 1 to n. The previous relation is then transformed into

$$\sigma_{\mu\lambda}(\rho_\mu,\rho_\lambda)\frac{\partial}{\partial\rho_\kappa}[\hat{\Xi}_{\lambda\nu}(\{\rho_\mu\})]\sigma_{\nu\sigma}(\rho_\nu,\rho_\sigma) \\ +\frac{\partial}{\partial\rho_\kappa}[\sigma_{\mu\sigma}(\rho_\mu,\rho_\sigma)] = 0. \qquad (A4)$$

The cumulant generating functions for the n cells in $\mathcal{A}$ is given by

$$\hat{\varphi}(\{\lambda_\mu\}) = \lambda_\mu\tau_\mu - \frac{1}{2}\hat{\Xi}_{\mu\nu}\tau_\mu\tau_\nu, \qquad (A5)$$

with the stationary conditions

$$\lambda_\kappa = \hat{\Xi}_{\mu\kappa}\tau_\mu\frac{\mathrm{d}\tau_\kappa}{\mathrm{d}\rho_\kappa} + \frac{1}{2}\frac{\partial\hat{\Xi}_{\mu\nu}}{\partial\rho_\kappa}\tau_\mu\tau_\nu. \qquad (A6)$$

The purpose of the following calculation is to show that it is identical to the expression of $\varphi(\lambda_i)$ describing the cumulant generating function of the $n+m$ cells when the last $m-n$ values of λ_i are set to zero. In this case we have

$$\varphi(\{\lambda_\mu,0\}) = \lambda_\mu\tau_\mu - \frac{1}{2}\Xi_{ij}\tau_i\tau_j, \qquad (A7)$$

with the stationary conditions

$$\lambda_\kappa = \Xi_{i\kappa}\tau_i \frac{\mathrm{d}\tau_\kappa}{\mathrm{d}\rho_\kappa} + \frac{1}{2}\frac{\partial \Xi_{ij}}{\partial \rho_\kappa}\tau_i\tau_j, \tag{A8}$$

$$0 = \Xi_{ki}\tau_i \frac{\mathrm{d}\tau_k}{\mathrm{d}\rho_k} + \frac{1}{2}\frac{\partial \Xi_{ij}}{\partial \rho_k}\tau_i\tau_j, \tag{A9}$$

for k running from $n+1$ to $n+m$. The second set of constraints allows to determine the values of τ_i for $i \in [n+1, n+m]$ in terms of τ_ν. It is given by

$$\hat{\tau}_i = \sigma_{i\mu}\hat{\Xi}_{\mu\nu}\tau_\nu, \tag{A10}$$

where once again repeated Greek indices are summed over from 1 to n. This expression is actually valid for any values of i as when i is in the 1 to n range we identically have $\hat{\tau}_i = \tau_i$. One can indeed check that for this expression the two terms in Eq. (A9) are identically 0: indeed $\Xi_{ki}\hat{\tau}_i = \delta_{k\mu} = 0$ for $k \in [n+1, n+m]$ and $\partial\Xi_{ij}/\partial\rho_k\hat{\tau}_i\hat{\tau}_j = \partial\Xi_{ij}/\partial\rho_k\sigma_{i\mu}\hat{\Xi}_{\mu\nu}\tau_\nu\sigma_{j\mu'}\hat{\Xi}_{\mu'\nu'}\tau_{\nu'} = -\partial\sigma_{\mu\mu'}/\partial\rho_k\hat{\Xi}_{\mu\nu}\tau_\nu\hat{\Xi}_{\mu'\nu'}\tau_{\nu'} = 0$ for $k \in [n+1, n+m]$. Then replacing using this expression for the τ_i in Eq. (A8), one gets

$$\lambda_\kappa = \Xi_{i\kappa}\sigma_{i\mu}\hat{\Xi}_{\mu\nu}\tau_\nu \frac{\mathrm{d}\tau_\kappa}{\mathrm{d}\rho_\kappa} + \frac{1}{2}\frac{\partial \Xi_{ij}}{\partial \rho_\kappa}\sigma_{i\mu}\hat{\Xi}_{\mu\nu}\tau_\nu\sigma_{j\mu'}\hat{\Xi}_{\mu'\nu'}\tau_{\nu'}.$$

Its first term can be simplified using the definition of $\hat{\Xi}$ and the second by the subsequent use of Eqs. (A3) and (A4),

$$\begin{aligned}\frac{\partial \Xi_{ij}}{\partial \rho_\kappa}\sigma_{i\mu}\hat{\Xi}_{\mu\nu}\sigma_{j\mu'}\hat{\Xi}_{\mu'\nu'} &= -\frac{\partial}{\partial \rho_\kappa}\sigma_{\mu\mu'}\hat{\Xi}_{\mu\nu}\hat{\Xi}_{\mu'\nu'},\\ &= \frac{\partial \hat{\Xi}_{\kappa\sigma}}{\partial \rho_\kappa}\sigma_{\kappa\mu}\hat{\Xi}_{\mu\nu}\sigma_{\sigma\mu'}\hat{\Xi}_{\mu'\nu'},\\ &= \frac{\partial \hat{\Xi}_{\nu\nu'}}{\partial \rho_\kappa},\end{aligned} \tag{A11}$$

so that the expression of λ_κ coincides with the expression (A6). Finally $\hat{\tau}_\mu = \tau_\mu$ ensures that the property (A1) is valid.

APPENDIX B: INTEGRATION IN THE COMPLEX PLANE

1. Numerical algorithm

The computation of the one-point PDF relies on the following expression:

$$P(\hat{\rho}) = \int_{-\mathrm{i}\infty}^{+\mathrm{i}\infty} \frac{\mathrm{d}\lambda}{2\pi \mathrm{i}} \exp(-\lambda\hat{\rho} + \varphi(\lambda)), \tag{B1}$$

where we explicitly denote $\hat{\rho}$ as the value of the density for which we want to compute the PDF. This is to distinguish it from the variable ρ that enters in the calculation of $\varphi(\lambda)$ out of the Legendre transform of $\Psi(\rho)$. The idea to achieve fast convergence of the integral is to follow a path in the complex plane where the argument of the exponential in Eq. (B1) is real. The starting point of the calculation is $\rho = \rho_s$. When $\hat{\rho}$ is small enough (in the regular region) then we simply have $\rho_s = \hat{\rho}$ otherwise one should take $\rho_s = \rho_c$. At this very location, two lines of vanishing imaginary parts of $-\lambda\hat{\rho} + \varphi(\lambda)$ cross, one along the real axis (obviously) and one parallel to the imaginary axis (precisely because we are at a saddle point position). The idea is then to build, step by step, a path by imposing

$$\delta[\varphi(\lambda) - \lambda\hat{\rho}] \in \mathbb{R}. \tag{B2}$$

This condition can be written as an infinitesimal variation of λ. Recalling that $\mathrm{d}\varphi(\lambda)/\mathrm{d}\lambda = \rho(\lambda)$, for each step we have to impose

$$(\rho - \hat{\rho})\delta\lambda \in \mathbb{R}, \tag{B3}$$

which in turns can be obtained by imposing that the complex argument of $(\delta\rho)$ is that of $[(\rho - \hat{\rho})\mathrm{d}^2\Psi/\mathrm{d}\rho^2]^*$. This is what we implement in practice. Accurate prediction for the PDFs are obtained with about 50 points along the path line that is illustrated on Fig. 13.

2. The large density tails

The derivation of the rare event tail of the density PDF for large positive densities is based on the inverse Laplace transform of the generating function $\varphi(\lambda)$ when it is dominated by its singular part, i.e. for $\lambda \approx \lambda_c$. In this case the complex plane contour is pushed along the real axis wrapping around the singular value λ_c as depicted on Fig. 14.

The general form for the density PDF given by Eq. (B1) is expressed using the form (43) following the path shown on Fig. 14. As the contributions from the two branches of the path lines are complex conjugate, it eventually leads to the form

$$\begin{aligned}P(\hat{\rho}) \approx \Im\Big\{&\int_{\mathrm{i}\epsilon+\lambda_c}^{\mathrm{i}\epsilon+\infty}\frac{\mathrm{d}\lambda}{\pi}\exp[\varphi_c - \lambda_c\hat{\rho} - (\lambda - \lambda_c)(\hat{\rho} - \rho_c)]\\ &\times[1 + a_{3/2}(\lambda - \lambda_c)^{3/2} + \cdots]\Big\},\end{aligned} \tag{B4}$$

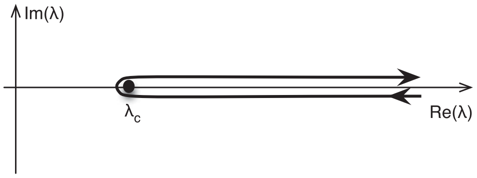

FIG. 14. The path line in the λ complex plane for the computation of the large density asymptotic forms.

where we keep only the dominant singular part in $\varphi(\lambda)$ and where $\Im$ denotes the imaginary part. This integral can easily be computed and it leads to

$$P(\hat\rho) \approx \exp\left(\varphi_c - \lambda_c\hat\rho\right)\left(\frac{3\Im(a_{\frac{3}{2}})}{4\sqrt{\pi}(\hat\rho-\rho_c)^{5/2}} + \cdots\right). \tag{B5}$$

Subleading contributions can be computed in a similar way when $\exp(\varphi(\lambda))$ is expanded to higher order. Note that by symmetry, only half integer terms that appear in this expansion will actually contribute.

APPENDIX C: THE CONSTRAINED VARIANCE

In this appendix we complement the calculations started in Sec. IV E where we computed the expected slope under a local density constraint. Pursuing along the same line of calculations, the variance of $\hat\rho_2$ given $\hat\rho_1$ can be computed from the conditional value of $\hat\rho_2^2$. It is given by the second derivative of the moment generating function, and is therefore given by

$$\begin{aligned}\int \mathrm{d}\hat\rho_2\hat\rho_2^2 P(\hat\rho_1,\hat\rho_2) &\\ = \int_{-\mathrm{i}\infty}^{+\mathrm{i}\infty}\frac{\mathrm{d}\lambda_1}{2\pi\mathrm{i}}&\left[\frac{\partial^2\varphi(\lambda_1,\lambda_2)}{\partial\lambda_2^2}\bigg|_{\lambda_2=0}\right.\\ &\left.+\left(\frac{\partial\varphi(\lambda_1,\lambda_2)}{\partial\lambda_2}\bigg|_{\lambda_2=0}\right)^2\right]\exp(-\lambda_1\hat\rho_1+\varphi(\lambda_1)).\end{aligned}$$

The calculation of its approximate form in the low-ρ saddle point limit is a bit more cumbersome. Indeed, in the low variance limit in which this approximation is derived the two terms in the square brackets are not of the same order, the first being subdominant with respect the second. It is nonetheless possible to compute the resulting cumulant in the low density limit. Formally, differentiating Eq. (90) with respect to λ_2 we have

$$\frac{\partial^2\varphi(\lambda_1,\lambda_2)}{\partial\lambda_2^2} = \frac{\partial\rho_2(\lambda_1,\lambda_2)}{\partial\lambda_2}, \tag{C1}$$

from the Legendre stationary condition, which, after inversion of the partial derivatives, is formally given by

$$\frac{\partial^2\varphi(\lambda_1,\lambda_2)}{\partial\lambda_2^2} = \frac{\Psi_{,\rho_1\rho_1}}{\Psi_{,\rho_1\rho_1}\Psi_{,\rho_2\rho_2}-\Psi^2_{,\rho_1\rho_2}}, \tag{C2}$$

where $\Psi_{,\rho_i\rho_j} \equiv \partial^2\Psi/\partial\rho_i\partial\rho_j$ are calculated at the stationary point. On the other hand $\partial\varphi(\lambda_1,\lambda_2)/\partial\lambda_2$ can be expanded as

$$\begin{aligned}\frac{\partial\varphi(\lambda_1,\lambda_2)}{\partial\lambda_2} &= \varphi(\lambda_s,0)+(\lambda_1-\lambda_s)\\ &\quad\times\frac{\partial^2\varphi(\lambda_1,\lambda_2)}{\partial\lambda_2\partial\lambda_1}+\frac{1}{2}(\lambda_1-\lambda_s)^2\frac{\partial^3\varphi(\lambda_1,\lambda_2)}{\partial\lambda_2\partial\lambda_1^2}+\cdots\end{aligned} \tag{C3}$$

near the saddle point value λ_s. The integration of $\partial\varphi(\lambda_1,\lambda_2)/\partial\lambda_2$ in the complex plane therefore leads to a correction from the $(\lambda_1-\lambda_s)^2$ term. It can be verified though that this contribution vanishes when one takes the cumulant. The integration of $(\partial\varphi(\lambda_1,\lambda_2)/\partial\lambda_2)$ however leads to an extra term due to the second term in the previous expansion. The resulting term reads $[\partial^2\varphi/\partial\lambda_2\partial\lambda_1]^2/\partial^2\varphi/\partial\lambda_1^2$, so that

$$\begin{aligned}\langle\rho_2^2\rangle_{\rho_1}-\langle\rho_2\rangle^2_{\rho_1} &= \frac{\partial^2\varphi}{\partial\lambda_1^2}-\left[\frac{\partial^2\varphi}{\partial\lambda_2\partial\lambda_1}\right]^2\Big/\frac{\partial^2\varphi}{\partial\lambda_1^2}\\ &= \left[\frac{\partial^2\varphi}{\partial\lambda_1^2}\frac{\partial^2\varphi}{\partial\lambda_2^2}-\left(\frac{\partial^2\varphi}{\partial\lambda_1\partial\lambda_2}\right)^2\right]\Big/\frac{\partial^2\varphi}{\partial\lambda_1^2},\end{aligned} \tag{C4}$$

which can be rewritten more compactly as

$$\langle\hat\rho_2^2\rangle_{\hat\rho_1}-\langle\hat\rho_2\rangle^2_{\hat\rho_1} = 1/\Psi_{,\rho_2\rho_2}|_{\hat\rho_1,\bar\rho_2(\hat\rho_1)}, \tag{C5}$$

when expressed in terms of Ψ.

APPENDIX D: SIMULATIONS

For the purpose of this paper, we have carried out a dark matter simulation with GADGET2 [66]. This simulation is characterized by the following ΛCDM cosmology: $\Omega_\mathrm{m}=0.265$, $\Omega_\Lambda=0.735$, $n=0.958$, $H_0=70$ km $\times$ $\mathrm{s}^{-1}\times\mathrm{Mpc}^{-1}$ and $\sigma_8=0.8$, $\Omega_b=0.045$ within one standard deviation of Wilkinson Microwave Anisotropy Probe 7 results [67]. The box size is 500 Mpc/h sampled with 1024^3 particles, the softening length 24 kpc/h. Initial conditions are generated using MPGRAFIC [68]. The variances and running indexes are measured from the theoretical power spectra produced by MPGRAFIC. Snapshots are saved for $z=0, 0.65, 0.97, 1.46, 2.33$ and 3.9. An Octree is built for each snapshot, which allows us to count very efficiently all particles within a given sequence of concentric spheres of radii between $R=4,5\ldots$ up to 18 Mpc/h. The center of these spheres is sampled regularly on a grid of 10 Mpc/h aside, leading to 117 649 estimates of the density per snapshot. All histograms drawn in this paper are derived from these samples. Note that the cells overlap for radii larger than 10 Mpc/h.

APPENDIX E: SYSTEMATIC COMPARISONS WITH SIMULATION

We collect here figures that are too large to be put in the main text.

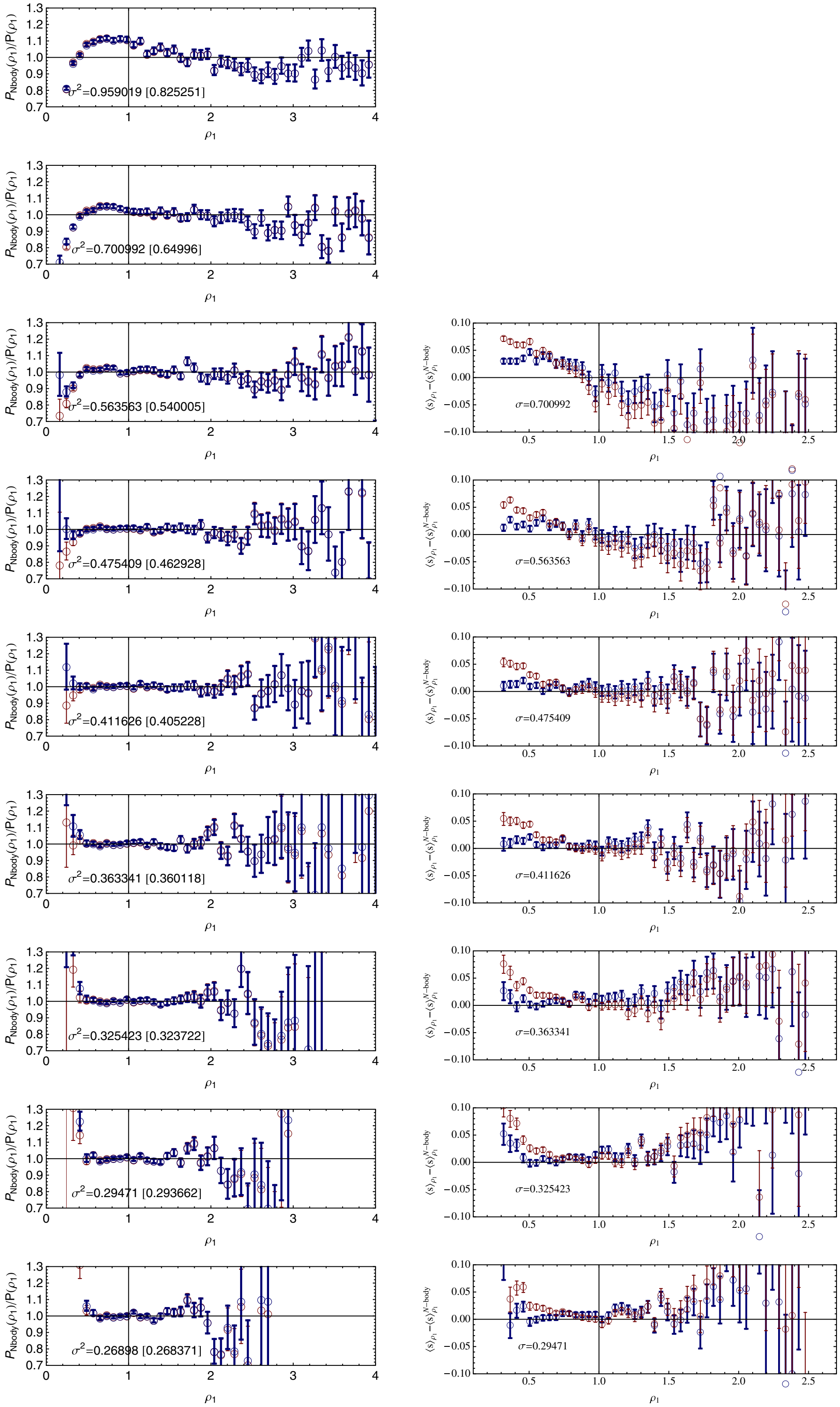

FIG. 15 (color online). (Left panels) The residuals of the expected density PDF from smoothing scale of $R_1 = 4$ (top panel) to $R_1 = 20h^{-1}$ Mpc. This is for $z = 0.97$ (same convention as in Fig. 3). The values of σ^2 at the smoothing scale is given in the inset. The value in square brackets is the linear value. (Right panels) The residuals for the expected average profile between scale R_1 and $R_2 = R_1 + 1h^{-1}$ Mpc. From top to bottom we have $R_1 = 6$ to $18h^{-1}$ Mpc. Same convention as in Fig. 8.

[1] See http://bigboss.lbl.gov, https://www.darkenergysurvey.org, http://pan-starrs.ifa.hawaii.edu, and http://www.lsst.org.

[2] R. Laureijs, J. Amiaux, S. Arduini, J.-L. Augueres, J. Brinchmann, R. Cole, M. Cropper, C. Dabin, L. Duvet, A. Ealet *et al.*, arXiv:1110.3193.

[3] See http://sci.esa.int/euclid, http://snap.lbl.gov, and http://jdem.lbl.gov.

[4] S. F. Daniel, E. V. Linder, T. L. Smith, R. R. Caldwell, A. Cooray, A. Leauthaud, and L. Lombriser, Phys. Rev. D **81**, 123508 (2010).

[5] A. F. Heavens, T. D. Kitching, and L. Verde, Mon. Not. R. Astron. Soc. **380**, 1029 (2007).

[6] F. Bernardeau, S. Colombi, E. Gaztañaga, and R. Scoccimarro, Phys. Rep. **367**, 1 (2002).

[7] M. Crocce and R. Scoccimarro, Phys. Rev. D **73**, 063519 (2006).

[8] A. Taruya and T. Hiramatsu, Astrophys. J. **674**, 617 (2008).

[9] M. Pietroni, J. Cosmol. Astropart. Phys. 10 (2008) 036.

[10] M. Crocce, R. Scoccimarro, and F. Bernardeau, Mon. Not. R. Astron. Soc. **427**, 2537 (2012).

[11] A. Taruya, F. Bernardeau, T. Nishimichi, and S. Codis, Phys. Rev. D **86**, 103528 (2012).

[12] J. J. M. Carrasco, M. P. Hertzberg, and L. Senatore, J. High Energy Phys. 09 (2012) 082.

[13] J. M. Bardeen, J. R. Bond, N. Kaiser, and A. S. Szalay, Astrophys. J. **304**, 15 (1986).

[14] J. R. Gott III, Publ. Astron. Soc. Pac. **100**, 1307 (1988).

[15] K. R. Mecke, T. Buchert, and H. Wagner, Astron. Astrophys. **288**, 697 (1994).

[16] S. Colombi, D. Pogosyan, and T. Souradeep, Phys. Rev. Lett. **85**, 5515 (2000).

[17] C. Gay, C. Pichon, and D. Pogosyan, Phys. Rev. D **85**, 023011 (2012).

[18] T. Matsubara, Astrophys. J. Lett. **434**, L43 (1994).

[19] S. Codis, C. Pichon, D. Pogosyan, F. Bernardeau, and T. Matsubara, Mon. Not. R. Astron. Soc. **435**, 531 (2013).

[20] R. Balian and R. Schaeffer, Astron. Astrophys. **220**, 1 (1989).

[21] F. Bernardeau, Astrophys. J. **392**, 1 (1992).

[22] F. Bernardeau, Astron. Astrophys. **291**, 697 (1994).

[23] R. Juszkiewicz, F. R. Bouchet, and S. Colombi, Astrophys. J. Lett. **412**, L9 (1993).

[24] F. Bernardeau, Astrophys. J. **433**, 1 (1994).

[25] C. M. Baugh, E. Gaztanaga, and G. Efstathiou, Mon. Not. R. Astron. Soc. **274**, 1049 (1995).

[26] F. Bernardeau, Astron. Astrophys. **312**, 11 (1996).

[27] F. Bernardeau, Astron. Astrophys. **301**, 309 (1995).

[28] F. Bernardeau and P. Valageas, Astron. Astrophys. **364**, 1 (2000).

[29] P. Valageas, Astron. Astrophys. **382**, 412 (2002).

[30] G. Lavaux and B. D. Wandelt, Astrophys. J. **754**, 109 (2012).

[31] P. M. Sutter, G. Lavaux, B. D. Wandelt, and D. H. Weinberg, Astrophys. J. **761**, 44 (2012).

[32] K. Bolejko and R. A. Sussman, Phys. Lett. B **697**, 265 (2011).

[33] R. van de Weygaert and E. Platen, Int. J. Mod. Phys. Conf. Ser. **01**, 41 (2011).

[34] M. A. Aragon-Calvo, R. van de Weygaert, P. A. Araya-Melo, E. Platen, and A. S. Szalay, Mon. Not. R. Astron. Soc. **404**, L89 (2010).

[35] G. Lavaux and B. D. Wandelt, Mon. Not. R. Astron. Soc. **403**, 1392 (2010).

[36] M. A. Aragon-Calvo and A. S. Szalay, Mon. Not. R. Astron. Soc. **428**, 3409 (2013).

[37] Specifically, we expect perturbation theory to break down later in low density regions; we also expect these regions to probe smaller Lagrangian scales.

[38] J. Binney, N. Dowrick, A. Fisher, and M. Newman, *The Theory of Critical Phenomena* (Oxford University, New York, 1992).

[39] C. Heyde, J. R. Stat. Soc. Ser. B **25**, 392 (1963).

[40] It is to be noted however that it is not necessarily defined for any real values of λ as one expects for instance that the one-point density PDF develops an exponential cutoff, $\mathcal{P}(\rho) \sim \exp(-\lambda_c \rho)$, which implies that $\varphi(\lambda)$ is undefined when $\lambda > \lambda_c$.

[41] This comes from a simple counting of lines: one needs at least $p-1$ lines to connect p points which in turns forces the sum of orders at which each factor is computed to be $2(p-1)$; see [6,21,22,42].

[42] J. N. Fry, Astrophys. J. **279**, 499 (1984).

[43] P. J. E. Peebles, *The Large-Scale Structure of the Universe*, Princeton Series in Physics, edited by S. B. Treiman (Princeton University, Princeton, NJ, 1980).

[44] F. Bernardeau, *Cosmologie: Des Fondements Théoriques aux Observations* (EDP Sciences, Les Ulis, France, 2007).

[45] We could choose $\nu = 3/2$ in order to reproduce the low density asymptotic behavior of the exact solution.

[46] We implicitly assume throughout this paper that the initial conditions are adiabatic so that the perturbations developed out of a single scalar field degree of freedom.

[47] This is actually a superfluous hypothesis but we adopt it for convenience. Transient effects form mildly non-Gaussian initial conditions can for instance be taken into account in this formalism as shown in [48].

[48] P. Valageas, Astron. Astrophys. **382**, 431 (2002).

[49] This relation is *a priori* time dependent but we will omit it in the following.

[50] This inversion is possible as long as $\Psi(\{\tau_k\})$ is a convex function of ρ_k which in practice means before shell crossing.

[51] Thus, if we define $\varphi_{\rm init}(\{\lambda_k\})$ as the cumulant generating function of the density contrasts at initial time, we have $\Psi_{\rm init}(\{\rho_k\}) = \sum_i \rho_i \lambda_i - \varphi_{\rm init}(\{\lambda_k\})$, with $\rho_i = \partial\varphi_{\rm init}/\partial\lambda_i$. It is easy to check that for Gaussian initial conditions, $\varphi_{\rm init}(\{\lambda_i\}) = \sum_i \lambda_i + \frac{1}{2}\sum_{ij}\Sigma_{ij}\lambda_i\lambda_j$, which leads to the expression (25) given previously for Ψ.

[52] F. Bernardeau and R. Schaeffer, Astron. Astrophys. **255**, 1 (1992).

[53] It is beyond the scope of this paper to discuss the validity of this inversion and how it can generally be implemented. Interested readers can find detailed discussions of this construction in [20] in the context of cosmological density PDF and counts in cells statistics, where it has been carried out in particular for the one-point PDF, the properties of which are crucially related to the analytical properties of the cumulant generating function.

[54] In [52] this inversion was initially performed for models of nonlinear clustering (hierarchical models) taking advantage of the general results presented in [20]. The same techniques were later employed in the context of perturbation theory calculations. For all these constructions, the analytical properties of the cumulant generating function follow from the structure of the stationary condition.

[55] Note that in practice π_3 is negative and that only the nonregular parts appearing in the expansion of $\exp(\varphi(\lambda))$ will contribute.

[56] The change of sign in Eq. (45) comes from the path that is *orthogonal* to the real axis.

[57] F. Bernardeau, Astrophys. J. Lett. **390**, L61 (1992).

[58] An alternative approach would be to use predicted amplitude form direct next-to-leading-order perturbation theory calculations. We leave this option for further studies.

[59] F. Bernardeau and L. Kofman, Astrophys. J. **443**, 479 (1995).

[60] The difference can be, to a large extent, interpreted by the nonlinear growth of the reduced skewness.

[61] In practice this is achieved via a series expansion inversion of Eq. (24) then plugged in Eq. (23).

[62] Again when n_s is less than -1 in case of a power law spectrum.

[63] The location of the resulting critical line is only weakly sensitive to the threshold we choose.

[64] It involves expressing P as a function of φ, expressing ρ_2 integrating over ρ_2 and using Cauchy's theorem.

[65] A similar experiment for three-cells of size $R = 11, 12$ and 13 Mpc/h was carried out, producing similar results.

[66] V. Springel, Mon. Not. R. Astron. Soc. **364**, 1105 (2005).

[67] E. Komatsu, K. M. Smith, J. Dunkley, C. L. Bennett, B. Gold, G. Hinshaw, N. Jarosik, D. Larson, M. R. Nolta, L. Page *et al.*, Astrophys. J. Suppl. Ser. **192**, 18 (2011).

[68] S. Prunet, C. Pichon, D. Aubert, D. Pogosyan, R. Teyssier, and S. Gottloeber, Astophys. J. Suppl. Ser. **178**, 179 (2008).